## STRUCTURAL BIOLOGY

# Development of enhanced HIV-1 non-nucleoside reverse transcriptase inhibitors with improved resistance and pharmacokinetic profiles

Zhao Wang[1,2]†, Shawn Rumrill[3]†, Dongwei Kang[1,2]†, Samuel Desta Guma[1,2]†, Da Feng[1,2], Erik De Clercq[4], Christophe Pannecouque[4], Chin Ho Chen[5]*, Eddy Arnold[3]*, Francesc Xavier Ruiz[3]*, Xinyong Liu[1,2]*, Peng Zhan[1,2]*

HIV-1 infection is a manageable chronic condition, with non-nucleoside HIV-1 reverse transcriptase inhibitors (NNRTIs) remaining a cornerstone of antiretroviral therapy. Nevertheless, drug resistance to existing therapeutics is a serious and immediate concern. Using structure-based and scaffold-hopping approaches, we designed evolved diarylpyrimidine analogs targeting reverse transcriptase (RT), exploiting chemical space surrounding the NNRTI-binding pocket. We identified compounds **5i3** and **5e2**, with robust antiviral efficacy against wild-type HIV-1 and rilpivirine-resistant strains. Encouragingly, in vitro selection of mutant strains with **5i3** took 39 passages to select resistance, with no phenotypic cross-resistance observed with known RT drugs. Co-crystal structures of wild-type and mutant RT with **5i3** and **5e2** revealed their resilience toward resistance mutations due to enhanced conformational flexibility and positional adaptability. **5i3** exhibited good pharmacokinetic properties and favorable safety profiles, without substantial cytochrome P450 inhibition, and excellent oral bioavailability. These derivatives represent a promising scaffold for the development of anti-HIV drugs.

## INTRODUCTION

AIDS, caused by HIV-1, is still one of the most serious infectious diseases that threatens public health worldwide (*1*, *2*). The introduction of highly active antiretroviral therapy (HAART) has successfully curbed the spread of HIV, but the rapid emergence of drug resistance considerably compromised its clinical application (*3*, *4*). HIV-1 reverse transcriptase (RT) holds far-reaching therapeutic promise because of its unique role during the viral life cycle (*5–7*). As an essential class of anti-HIV therapeutics, non-nucleoside reverse transcriptase inhibitors (NNRTIs) are widely used in the HAART regimens because of their relatively potent activity, modest toxicity, and high specificity. NNRTIs non-competitively bind to an allosteric site [i.e., NNRTI-binding pocket (NNIBP)] about 10 Å away from the polymerase active site, resulting in distortion of the catalytic active site and eventually leading to inhibition of the reverse transcription process (*8*, *9*).

To date, there are six NNRTIs approved by the US Food and Drug Administration (FDA). However, first-generation NNRTIs, including nevirapine (NVP), delavirdine, and efavirenz (EFV), generally suffer from a low genetic barrier to resistance. High levels of resistance can be rapidly induced by a single–amino acid point mutation, as exemplified by the two most prevalent single mutants: K103N and Y181C (*10*, *11*). As shown in Fig. 1A, second-generation NNRTIs etravirine (ETR) and rilpivirine (RPV) belong to the diarylpyrimidine (DAPY) family, which represents the most powerful class of NNRTIs (*12*). Although the second-generation NNRTIs have a higher genetic barrier to resistance and exhibit potent inhibitory activity against most drug-resistant strains, the emergence of double-mutant or even triple-mutant strains after clinical treatment still greatly reduced their antiviral efficacy. Examples of these resistance mutations include K101P and Y181I for ETR and L100I, K101E/P, E138K/G, Y181C/V, H221Y, and M230L for RPV (*13*, *14*).

Resistance-associated mutations generally reduce the binding affinity to the target by affecting interactions between inhibitors and their binding site, thereby conferring drug resistance (*15*, *16*). In the case of the resistance mutation K103N, a comparison of the unliganded wild-type (WT) and K103N mutant RT structures revealed that the side chain of N103 forms a hydrogen bond with the Y188 phenoxyl group that contributes to stabilizing the closed NNIBP, which may limit inhibitor entry (*17*, *18*). Another resistance mutation, K101P, can also affect the rate of entry into the NNIBP by perturbing the hydrogen-bonding network around the pocket because of the inability of the main-chain nitrogen in the proline to form a hydrogen bond (*19*, *20*). Conversely, the V108 side chain located behind Y188 does not form direct interactions with NNRTIs. Instead, the V108I mutation perturbs the nearby Y181 and Y188 phenoxyl ring conformations, potentially reducing stabilization from π-π stacking interactions between NNRTIs and these aromatic residues (*21*, *22*).

Genotype-phenotype correlation analysis of HIV-1 subtype B clinical infection indicated that the K101P mutation confers substantial resistance to existing NNRTIs (*23*). Generally, the K101P mutation alone resulted in a substantial reduction in efficacy, up to 243-fold for RPV, >50-fold for EFV, and about five-fold for ETR. Because the K101P mutation appears to contribute to severe cross-resistance to almost all NNRTIs, the possibility of treatment failure

[1]Department of Medicinal Chemistry, Key Laboratory of Chemical Biology (Ministry of Education), School of Pharmaceutical Sciences, Cheeloo College of Medicine, Shandong University, Jinan 250012, Shandong, PR China. [2]China-Belgium Collaborative Research Center for Innovative Antiviral Drugs of Shandong Province, Jinan 250012, Shandong, PR China. [3]Center for Advanced Biotechnology and Medicine, and Department of Chemistry and Chemical Biology, Rutgers University, Piscataway, NJ 08854, USA. [4]Rega Institute for Medical Research, Laboratory of Virology and Chemotherapy, K.U. Leuven, Herestraat 49 Postbus 1043 (09.A097), B-3000 Leuven, Belgium. [5]Surgical Oncology Research Facility, Duke University Medical Center, Box 2926, Durham, NC 27710, USA.
*Corresponding author. Email: chinho.chen@duke.edu (C.H.C.); arnold@cabm.rutgers.edu (E.A.); xavier@cabm.rutgers.edu (F.X.R.); xinyongl@sdu.edu.cn (X.L.); zhanpeng1982@sdu.edu.cn (P.Z.)
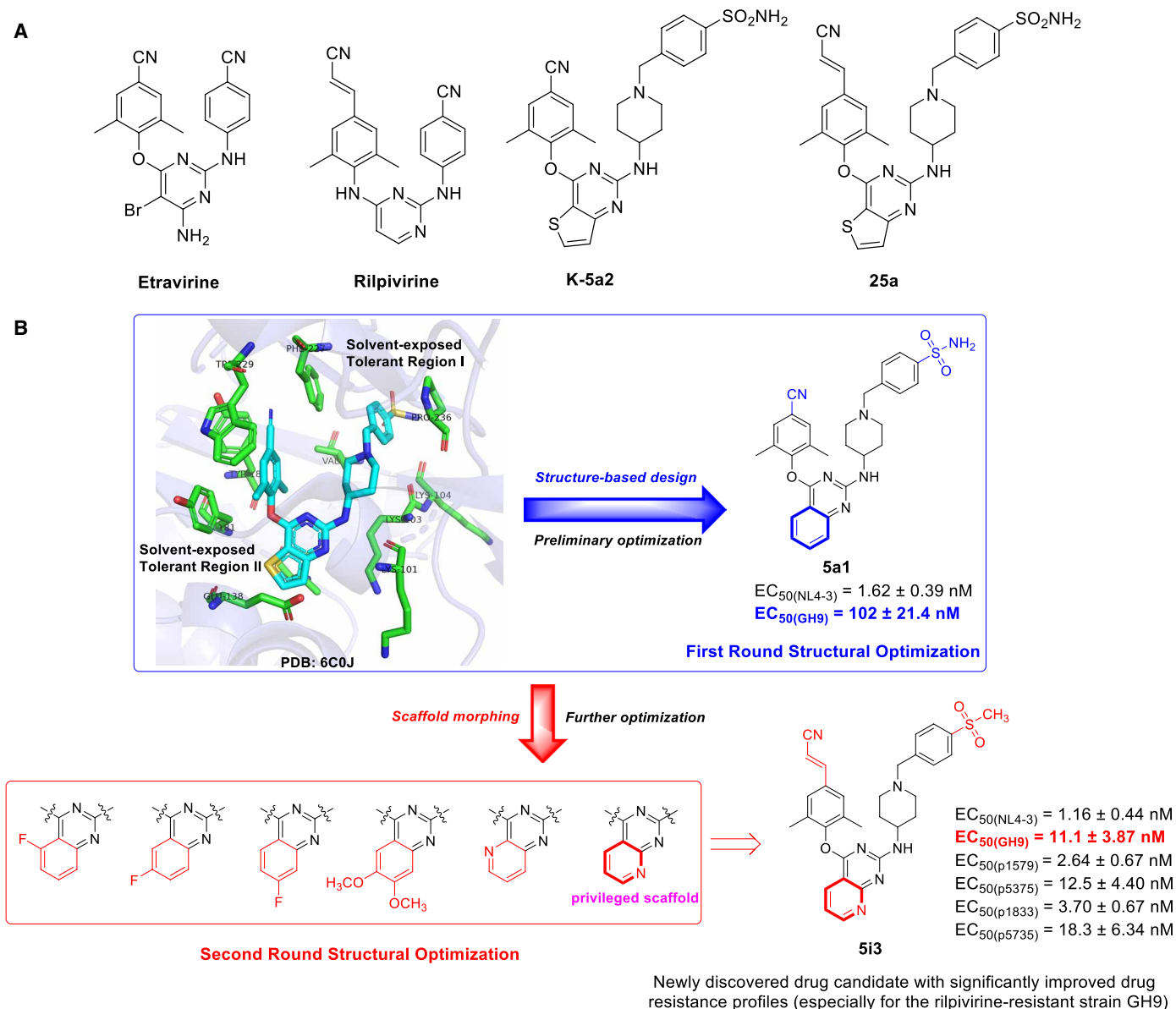†These authors contributed equally to this work.

**Fig. 1. Rational design of DAPY-evolved derivatives as potent HIV-1 inhibitors.** (**A**) Chemical structures of the FDA-approved NNRTIs etravirine (ETR) and rilpivirine (RPV) and the lead compounds K-5a2 and 25a. (**B**) Illustration of the structure-based design strategy and molecular optimization campaign of DAPY-evolved derivatives in this work.

will greatly increase once the K101P-carrying virus spreads (*24*, *25*). However, the K103N mutation is the most prevalent resistance-associated mutation in clinical practice, occurring in about 40 to 60% of NNRTI-resistant strains. The K103N mutation markedly reduces the efficacy of first-generation NNRTIs, resulting in about 20-fold and 50-fold reduction in susceptibility to EFV and NVP, respectively (*26*, *27*). Regarding the V108I mutation, intermediate resistance to doravirine (DOR) has been detected in vitro and in vivo (*28–30*). Cross-resistance between NNRTIs has been reported in various studies, and treatment-experienced patients are more likely to carry mutations that are resistant to ETR and RPV (*31*, *32*). Among emerging NNRTI-resistant strains of clinical significance, the triple-mutant strain GH9 (K101P/K103N/V108I) conferred >162-fold resistance to RPV, about 18-fold resistance to ETR, and

up to 12,931-fold resistance to EFV (*33–35*). We used the GH9 strain (containing the previous three NNRTI-resistance mutations) as a benchmark of highly cross-resistant strain to target in the search for potent NNRTIs with improved resistance profiles and better pharmacological properties.

In previous efforts to develop NNRTIs with improved resistance profiles, two potent DAPY-type NNRTIs, K-5a2 and 25a, were discovered in our laboratory (Fig. 1A) (*36*, *37*). Although both K-5a2 and 25a exhibited overall improved antiviral activities compared to ETR, they all suffered from detrimental human *ether-à-go-go–related gene* (hERG) inhibition [median inhibitory concentration (IC$_{50}$) = 0.13 and 0.18 μM] and unfavorable oral bioavailability (*F* = 22.9 and 16.2%) (*38*, *39*). Co-crystal structures of RT in complexes with K-5a2 and 25a illustrated that the structural flexibility and extensive

hydrogen-bonding networks account for their improved resistance profiles (20). Notably, the two solvent-exposed regions of NNIBP, tolerant region I (groove) and tolerant region II (entrance), provide substantial opportunities for expansion and chemically diverse modification of DAPY derivatives to increase target affinity and improve pharmacokinetic (PK) properties (40).

On the basis of insights into the mechanism of action of multiple NNRTI-resistant mutations, we applied a structure-based drug design strategy to maximize protein-ligand interactions by fully occupying the binding site to overcome drug resistance (15, 41, 42). In the present work, the central thiophene[3,2-d]pyrimidine scaffold was first replaced by a quinazoline core via a scaffold-hopping strategy in the hope that the larger quinazoline ring could effectively occupy the chemical space of solvent-exposed regions and establish more interactions with surrounding residues. Meanwhile, the privileged 2,4,6-trisubstituted phenol moiety and piperidine-substituted benzyl motif were retained. The preliminary biological evaluation results indicated that compound 5a1 exhibited moderate activity against HIV-1 WT and GH9 mutant strains. In continuation of our exploration, structurally diverse aromatic rings were introduced into the pyrimidine core to improve drug resistance profiles further. On the basis of the preliminarily established structure-activity relationships (SARs), the privileged cyanovinyl group was also installed at the two preferred quinazoline and pyrido[2,3-d]pyrimidine rings to develop additional $\pi$-$\pi$ stacking interactions with the highly conserved residues F227 and W229. Eventually, the pyrido[2,3-d]pyrimidine derivative 5i3 was identified as a promising drug candidate with improved resistance profiles and favorable drug-like properties (Fig. 1B). Herein, we report the design, synthesis, biological characterization, druggability evaluation, and crystallographic studies of those DAPY-evolved derivatives.

## RESULTS

### Chemical synthesis of target compounds

The synthetic protocols for the designed derivatives are outlined in figs. S9 and S10 (43, 44). Initially, the treatment of commercially available 2,4-dichloroquinazoline (1a) with 3,5-dimethyl-4-hydroxybenzonitrile or (E)-3-(4-hydroxy-3,5-dimethylphenyl)acrylonitrile afforded intermediates 2a or 2f, which then underwent a nucleophilic substitution reaction with 4-(tert-butoxycarbonyl)-aminopiperidine to provide intermediates 3a or 3f. Subsequent deprotection of the butoxycarbonyl group with trifluoroacetic acid gave the corresponding analogs 4a and 4f. Last, 4a and 4f were treated with various substituted benzyl chlorides (or bromines) in the presence of potassium carbonate to produce the target compounds 5a1–20 and 5f1–3. Similarly, other target compounds were synthesized from various commercially available starting materials.

### Anti-HIV activity evaluation and SAR analysis

All target compounds were first evaluated for their anti–HIV-1 activity and cytotoxicity in TZM-bl cell cultures infected with WT HIV-1 strain (NL4-3). Selected compounds were further tested for their inhibitory potency against a panel of NNRTI-resistant strains, including GH9 (K101P/K103N/V108I), p1579 (E138G/H221Y/F227L/M230L), p5375 (A98G/K101E/E138K/Y181C), p1833 (A98G/K101E/Y181C/G190A), and p5735 (K101E/Y181V). The approved drugs ETR and RPV were chosen as reference drugs. The biological evaluation results of median effective concentration (EC$_{50}$; anti-HIV

potency), 50% cytotoxicity concentration (CC$_{50}$), and selectivity index (SI; CC$_{50}$/EC$_{50}$ ratio) are summarized in Tables 1 to 4.

With K-5a2 and 25a as lead compounds, our initial exploration kept the right-wing aminopiperidine moiety unchanged. At the same time, diverse hydrophilic or hydrophobic substituents were added to the piperidine around the tolerant region I. Other than maintaining the key hydrogen bonds with main-chain residues, introducing suitable groups may also improve the PK properties, including solubility, due to increased solvent exposure in this region. As shown in Table 1, all of the quinazoline derivatives 5a1–20 displayed moderate to excellent potency against the NL4-3 WT HIV-1 strain (EC$_{50}$ = 1.42 to 38.1 nM) but were slightly inferior to RPV (EC$_{50}$ = 0.96 nM). Additionally, no compounds displayed cytotoxicity at the maximum test concentrations. Compounds featuring hydrophilic groups in the phenyl ring yielded the most active potency, exemplified by 5a1 (-SO$_2$NH$_2$, EC$_{50}$ = 1.62 nM), 5a2 (-CONH$_2$, EC$_{50}$ = 1.82 nM), and 5a4 (-SO$_2$CH$_3$, EC$_{50}$ = 1.42 nM), indicating that the introduction of hydrophilic substituents in tolerant region I was more favorable for activity than hydrophobic substituents. Replacement of the hydrophilic groups with hydrophobic groups afforded compounds 5a7–17 with decreased potency (EC$_{50}$ = 11.4 to 38.1 nM). Furthermore, introducing hydrophilic substituents pyrimidine-2,4-dione or pyridine yielded the potent inhibitors 5a18 and 5a20 with EC$_{50}$ values of 2.04 and 3.20 nM, in agreement with our established SAR. In conclusion, based on the first round of SAR analysis, the presence of hydrophilic substituents on the phenyl ring enhanced the potency of the compounds. Specifically, substituents such as 4-SO$_2$NH$_2$, 4-CONH$_2$, and 4-SO$_2$CH$_3$ were preferred for tolerant region I (Fig. 2A).

After compound 5a1 was identified in the first round of SAR optimization as the lead compound, a series of structurally diverse rings varying in size and electronic nature was identified to replace the central quinazoline scaffold and explore the chemical space of tolerant region II. As depicted in Table 2, all compounds were effective against the NL4-3 WT HIV-1 strain, with EC$_{50}$ values ranging from 1.08 to 15.0 nM. Among them, 5e2 (EC$_{50}$ = 1.16 nM) and 5h2 (EC$_{50}$ = 1.08 nM) proved to be the two most active inhibitors, exhibiting activity comparable to that of RPV (EC$_{50}$ = 0.71 nM). However, these compounds showed greater or comparable cytotoxicity to RPV, resulting in lower SI values than RPV. Detailed SAR analysis could be derived from these analogs (Fig. 2B).

First, an overall comparison of the activities of the six subseries revealed a notable effect of the central scaffold on the potency. Taking the quinazoline ring as a reference, substituting a fluorine atom at different positions of the benzene ring afforded subseries 5b–5d with varying degrees of decreased activity. In particular, 5d3 (EC$_{50}$ = 15.0 nM) showed about 10-fold less potent activity than 5a1. Although the activity of 5e2 (EC$_{50}$ = 1.16 nM) was comparable to that of 5a1, the activities of other compounds in the subseries 5e decreased markedly, suggesting that the introduction of two bulky methoxyl groups may cause deleterious steric hindrance effects. In contrast, introducing nitrogen atoms can maintain the antiviral activity without changing the size of the central ring. Except for 5g1, other analogs of subseries 5g and 5h exhibited slightly greater or comparable potency to the 5a1. Moreover, the antiviral activity was also related to the position of the nitrogen atom, and the C$_8$-substitution (5h series) appeared to be modestly preferred over the C$_5$-substitution (5g series).

Second, a comparative analysis of each subseries of derivatives suggested that introducing three hydrophilic groups containing

**Table 1. Anti–HIV-1 (NL4-3) activity, cytotoxicity, and SI values of the target compounds 5a1–20.** Compd, compound.

| Compd | Ar | NL4-3 | | |
|---|---|---|---|---|
| | | $EC_{50}$ (nM)[*] | $CC_{50}$ (nM)[†] | SI[‡] |
| 5a1 | 4-SO$_2$NH$_2$-Ph | $1.62 \pm 0.39$ | >230 | >142 |
| 5a2 | 4-CONH$_2$-Ph | $1.82 \pm 0.61$ | >247 | >136 |
| 5a3 | 3-CONH$_2$-Ph | $8.55 \pm 2.86$ | >247 | >28.9 |
| 5a4 | 4-SO$_2$CH$_3$-Ph | $1.42 \pm 0.48$ | >231 | >163 |
| 5a5 | 4-CO$_2$CH$_3$-Ph | $28.4 \pm 8.93$ | >240 | >8.45 |
| 5a6 | 4-SO$_2$NH-cyclopropyl-Ph | $13.3 \pm 3.62$ | >215 | >16.2 |
| 5a7 | 4-NO$_2$-Ph | $14.8 \pm 4.46$ | >246 | >16.6 |
| 5a8 | 4-CH$_3$-Ph | $11.5 \pm 4.12$ | >261 | >22.7 |
| 5a9 | 4-Br-Ph | $34.4 \pm 12.3$ | >230 | >6.69 |
| 5a10 | 3-Br-Ph | $38.1 \pm 14.5$ | >231 | >6.06 |
| 5a11 | 2-Br-Ph | $33.9 \pm 8.43$ | >231 | >6.81 |
| 5a12 | 4-Cl-Ph | $29.0 \pm 7.80$ | >251 | >8.66 |
| 5a13 | 3-Cl-Ph | $25.3 \pm 7.82$ | >251 | >9.92 |
| 5a14 | 4-F-Ph | $29.3 \pm 7.43$ | >260 | >8.87 |
| 5a15 | 3-F-Ph | $25.3 \pm 7.97$ | >260 | >10.3 |
| 5a16 | 4-CN-Ph | $11.4 \pm 3.62$ | >256 | >22.5 |
| 5a17 | 2-CN-Ph | $27.8 \pm 6.45$ | >256 | >9.21 |
| 5a18 | Pyridine-4-yl | $2.04 \pm 0.71$ | >269 | >160 |
| 5a19 | Pyridine-2-yl | $16.9 \pm 5.32$ | >269 | >15.9 |
| 5a20 | Pyrimidine-2,4-dione | $3.20 \pm 0.94$ | >251 | >78.4 |
| RPV | – | $0.96 \pm 0.30$ | >341 | >355 |

*$EC_{50}$, concentration of compound that causes 50% inhibition of viral infection and determined in at least triplicate against HIV-1 virus in TZM-bl cell lines. NL4-3 is WT HIV-1 strain.    †$CC_{50}$, concentration that is cytotoxic to 50% of cells. The highest concentration of the tested compounds was 125 ng/ml.    ‡SI (selectivity index), the ratio of $CC_{50}/EC_{50}$.

hydrogen-bond donors/acceptors at the protein-solvent interface contributes to the anti–HIV-1 potency. However, no clear SAR was observed. Consequently, these privileged substituents were retained for further structural modifications.

On the basis of the known biological evaluation results from two rounds of exploration, a preliminary SAR analysis revealed that the quinazoline scaffold in the **5a** series and the pyrido[2,3-*d*]pyrimidine scaffold in the **5h** series exhibit enhanced potential for improving antiviral potency. In the third round of optimizations, we introduced a privileged cyanovinyl fragment into the left wing of these two scaffolds, aiming to extend the conjugated system and promote stronger π-π stacking interactions with the hydrophobic channel. As shown in Table 3, most of the compounds within the **5f** and **5i** subseries displayed potent inhibitory activity against WT ($EC_{50} = 1.16$ to 22.5 nM), except for compound **5i2**, which exhibited no activity ($EC_{50} > 46.8$ nM). This lack of activity may be attributed to an activity cliff effect, wherein structurally similar derivatives markedly reduce potency following minor structural modifications. Nevertheless, due to the lower cytotoxicity of RPV, it exhibited higher SI values compared to these compounds. Among these compounds, the most active inhibitor, **5i3**, showed antiviral efficacy comparable to RPV with an $EC_{50}$ value of 1.16 nM and no apparent cytotoxicity (Fig. 2C).

According to the above antiviral activity results, some representative compounds (**5a1**, **5a2**, **5a4**, **5a18**, **5e2**, and **5i3**) that potently inhibited the WT NL4-3 strain were further screened for their inhibitory activity against the triple-mutant strain GH9. As depicted in tables S1 and S4, all compounds were very effective in inhibiting the replication of the GH9 strain with $EC_{50}$ values in the range of 11.1 to 145. Intriguingly, the structurally modified compounds **5e2** ($EC_{50} = 22.1$ nM) and **5i3** ($EC_{50} = 11.1$ nM) both exhibited excellent antiviral activities at the double-digit nanomolar level, which were much better than those of ETR ($EC_{50} = 104$ nM) and RPV ($EC_{50} = 1707$ nM). Notably, the antiviral potency of **5i3** against the GH9 strain ($EC_{50} = 11.1$ nM) was about 9.4-fold higher than ETR and 154-fold higher than RPV.

The robust efficacy of **5e2** and **5i3** against the NL4-3 and GH9 strains prompted further evaluation of their antiviral activities toward several mutant strains to explore their resistance profiles, including p1579, p5375, p1833, and p5735 variants. As depicted in Table 4, both **5e2** and **5i3** exhibited potent activity ranging from sub-micromolar to nanomolar levels against a panel of NNRTI-resistant strains, with $EC_{50}$ values spanning from 2.64 to 165 nM. Consistent with the order of anti-GH9 activity, **5i3** ($EC_{50} = 2.64$ to 18.3 nM) also provided an overall higher inhibitory activity than **5e2** ($EC_{50} = 14.8$ to 165 nM) against these mutants, again emphasizing the significance of the pyrido[2,3-*d*]pyrimidine ring in maintaining activity against the resistance mutations. Notably, the antiviral activities of **5i3** [$EC_{50(p1579)} = 2.64$ nM, $EC_{50(p5375)} = 12.5$ nM, and $EC_{50(p1833)} = 3.70$ nM] were about 3 to 28 times more potent than that of ETR [$EC_{50(p1579)} = 74.9$ nM, $EC_{50(p5375)} = 37.6$ nM, and $EC_{50(p1833)} = 11.1$ nM] against the p1579, p5375, and p1833 mutant strains, respectively. As for the p5735 variant, although **5i3**
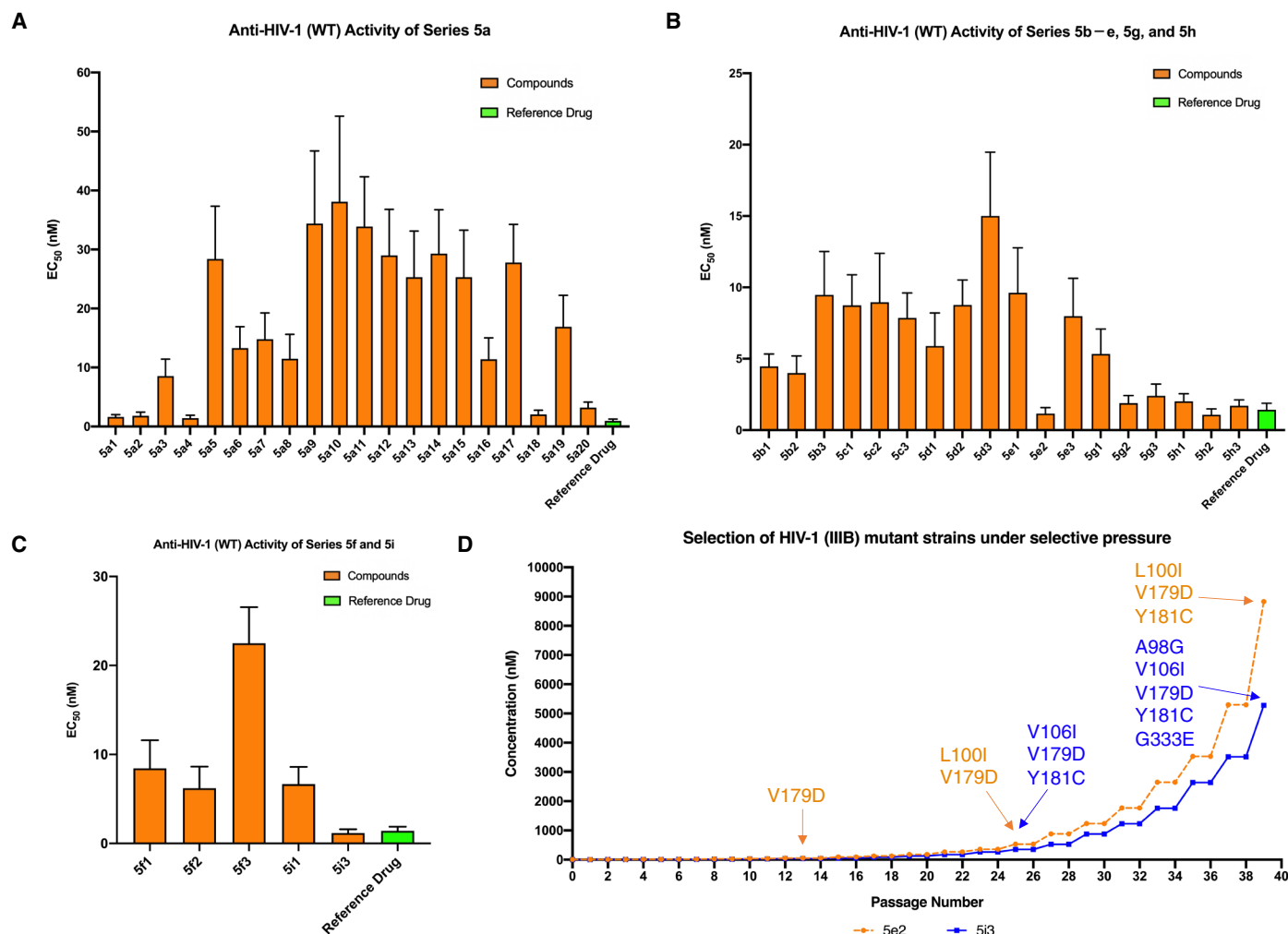
**Fig. 2. Biological activity evaluation results of the designed compounds.** (**A**) Anti–HIV-1 (WT) activity of series **5a**. (**B**) Anti–HIV-1 (WT) activity of series **5b–e**, **5g**, and **5h**. (**C**) Anti–HIV-1 (WT) activity of series **5f** and **5i**. (**D**) Kinetics of resistance development for the HIV-1 (IIIB) following selective pressure with compounds **5e2** and **5i3**. HIV-1 (IIIB) was cultured in MT-4 cells for 39 passages in the presence of increasing compound concentrations.

$[EC_{50(p5735)} = 18.3$ nM] displayed equipotent activity to ETR $[EC_{50(p5735)} = 14.3$ nM], it still yielded about ninefold improvement in potency compared to RPV $[EC_{50(p5735)} = 151$ nM].

In summary, systematic structure-based optimization campaigns were carried out by targeting tolerant region I/II and hydrophobic channel of RT; these efforts culminated in the discovery of compound **5i3** with improved resistance profiles and no apparent cytotoxicity, with $EC_{50}$ values ranging from 1.16 to 18.3 nM. **5i3** was endowed with exceptionally potent activity of 11.1 nM against the clinically highly resistant GH9 strain and proved worthy of further investigation.

## Selection of HIV-1 (IIIB) mutant strains under drug-selective pressure

Unlike the catalytic active site, the NNIBP is more heterogeneous as an allosteric binding site and can adapt to mutations without marked impairment of RT function or impact on viral fitness (*45*). Therefore, to further investigate the anti-resistance profiles of the potent HIV-1 inhibitors **5e2** and **5i3**, screening of HIV-1 mutant strains

was carried out in MT-4 cell cultures under drug-selective pressure. In the case of increasing the concentration of **5e2** and **5i3**, HIV-1 variants resistant to both compounds were obtained by continuous passage of the HIV-1 WT strain (IIIB) in MT-4 cells. The HIV-1 WT strain was cultured under the same test conditions in blank control experiments without drug-selective pressure. As illustrated in Fig. 2D and table S2, **5e2** was first selected for an RT amino acid mutation at the compound concentration of 53.0 nM when the virus was passaged for 13 rounds. After continuing 25 passages in MT-4 cells, more resistance mutations were obtained at 529.8 nM **5e2** and 352.0 nM **5i3**. Last, after 39 passages, the NNRTI-resistant strains were harvested and isolated at high concentrations of 8829.9 nM for **5e2** and 5279.6 nM for **5i3**.

## Progressive accumulation of mutations in the RT genes of selected HIV-1 strains

Resistance-associated mutations in the RT gene were further determined by isolating and sequencing proviral DNA from HIV-1 mutant strains compared to DNA sequences from the WT strain. These

**Table 2. Anti–HIV-1 (NL4-3) activity, cytotoxicity, and SI values of the target compounds 5b1–3, 5c1–3, 5d1–3, 5e1–3, 5g1–3, and 5h1–3.** Compd, compound.

| Compd | Ar | NL4-3 | | |
| --- | --- | --- | --- | --- |
| | | EC$_{50}$ (nM)$^*$ | CC$_{50}$ (μM)$^†$ | SI$^‡$ |
| 5b1 | 4-SO$_2$NH$_2$-Ph | 4.46 ± 0.87 | 14.8 ± 1.46 | 3318.4 |
| 5b2 | 4-CONH$_2$-Ph | 4.00 ± 1.20 | 15.2 ± 1.77 | 3800.0 |
| 5b3 | 4-SO$_2$CH$_3$-Ph | 9.47 ± 3.04 | 13.4 ± 1.28 | 1415.0 |
| 5c1 | 4-SO$_2$NH$_2$-Ph | 8.74 ± 2.14 | >53.5 | >6121.3 |
| 5c2 | 4-CONH$_2$-Ph | 8.96 ± 3.43 | >57.2 | >6383.9 |
| 5c3 | 4-SO$_2$CH$_3$-Ph | 7.86 ± 1.75 | 51.3 ± 4.47 | 6526.7 |
| 5d1 | 4-SO$_2$NH$_2$-Ph | 5.89 ± 2.32 | 12.8 ± 1.55 | 2173.2 |
| 5d2 | 4-CONH$_2$-Ph | 8.77 ± 1.75 | 13.9 ± 1.47 | 1584.9 |
| 5d3 | 4-SO$_2$CH$_3$-Ph | 15.0 ± 4.47 | 17.9 ± 2.32 | 1193.3 |
| 5e1 | 4-SO$_2$NH$_2$-Ph | 9.62 ± 3.15 | 8.79 ± 0.86 | 913.7 |
| 5e2 | 4-CONH$_2$-Ph | 1.16 ± 0.42 | 12.5 ± 1.15 | 10775.9 |
| 5e3 | 4-SO$_2$CH$_3$-Ph | 7.98 ± 2.66 | 9.14 ± 1.09 | 1145.4 |
| 5g1 | 4-SO$_2$NH$_2$-Ph | 5.33 ± 1.75 | 53.5 ± 4.59 | 10037.5 |
| 5g2 | 4-CONH$_2$-Ph | 1.89 ± 0.53 | 48.1 ± 5.12 | 25449.7 |
| 5g3 | 4-SO$_2$CH$_3$-Ph | 2.40 ± 0.83 | 43.3 ± 3.87 | 18041.7 |
| 5h1 | 4-SO$_2$NH$_2$-Ph | 2.02 ± 0.53 | 52.1 ± 4.97 | 25792.1 |
| 5h2 | 4-CONH$_2$-Ph | 1.08 ± 0.41 | 44.1 ± 3.55 | 40833.3 |
| 5h3 | 4-SO$_2$CH$_3$-Ph | 1.71 ± 0.41 | 40.0 ± 4.42 | 23391.8 |
| ETR | – | 1.42 ± 0.46 | ND$^§$ | ND |
| RPV | – | 0.71 ± 0.13 | >54.5 | >76760.6 |

*EC$_{50}$, concentration of compound that causes 50% inhibition of viral infection and determined in at least triplicate against HIV-1 virus in TZM-bl cell lines. NL4-3 is WT HIV-1 strain.    †CC$_{50}$, concentration that is cytotoxic to 50% of cells. The highest concentration of the tested compounds was 30 μg/ml.    ‡SI (selectivity index), the ratio of CC$_{50}$/EC$_{50}$.    §ND, not determined.

**Table 3. Anti–HIV-1 (NL4-3) activity, cytotoxicity, and SI values of the target compounds 5f1–3 and 5i1–3.** Compd, compound.

| Compd | Ar | NL4-3 | | |
| --- | --- | --- | --- | --- |
| | | EC$_{50}$ (nM)$^*$ | CC$_{50}$ (μM)$^†$ | SI$^‡$ |
| 5f1 | 4-SO$_2$NH$_2$-Ph | 8.44 ± 3.17 | 21.6 ± 2.46 | 2559.2 |
| 5f2 | 4-CONH$_2$-Ph | 6.20 ± 2.44 | 53.7 ± 5.26 | 8661.3 |
| 5f3 | 4-SO$_2$CH$_3$-Ph | 22.5 ± 4.05 | 33.1 ± 2.64 | 1471.1 |
| 5i1 | 4-SO$_2$NH$_2$-Ph | 6.67 ± 1.93 | >52.7 | >7901.0 |
| 5i2 | 4-CONH$_2$-Ph | >46.8 | 38.0 ± 4.68 | <812.0 |
| 5i3 | 4-SO$_2$CH$_3$-Ph | 1.16 ± 0.44 | 14.2 ± 1.93 | 12241.4 |
| ETR | – | 1.42 ± 0.46 | ND$^§$ | ND |
| RPV | – | 0.71 ± 0.13 | >54.5 | >76760.6 |

*EC$_{50}$, concentration of compound that causes 50% inhibition of viral infection and determined in at least triplicate against HIV-1 virus in TZM-bl cell lines. NL4-3 is WT HIV-1 strain.    †CC$_{50}$, concentration that is cytotoxic to 50% of cells. The highest concentration of the tested compounds was 30 μg/ml.    ‡SI (selectivity index), the ratio of CC$_{50}$/EC$_{50}$.    §ND, not determined.

are summarized in tables S3 to S5. The NNRTI-resistant strains selected during virus passaging under the selective pressure of **5e2** and **5i3** are referred to as **5e2**$^{res}$ and **5i3**$^{res}$ strains, respectively. Genotypic analysis of resistance selection after 13 passages indicated that the **5e2**$^{res}$ strain harbored the V179D mutation (concentration = 53.0 nM), whereas no mutation was observed yet for **5i3** (concentration = 35.2 nM) (table S3; Fig. 2D). After 25 passages, L100I and

V179D mutations were detected in the **5e2**$^{res}$ strain at 529.8 nM, while the **5i3**$^{res}$ strain carried V106I, V179D, and Y181C mutations at 352.0 nM (table S4). After 39 passages, the V179D and Y181C mutations emerged in both **5e2**$^{res}$ (concentration = 8829.9 nM) and **5i3**$^{res}$ (concentration = 5279.6 nM) strains. In addition, the **5e2**$^{res}$ strain carried the L100I substitution, while the **5i3**$^{res}$ strain also contained the A98G, V106I, and G333E mutations (table S5). Regarding the

**Table 4. Antiviral activity against NNRTI-resistant strains (GH9, p1579, p5375, p1833, and p5735) of selected compounds 5e2 and 5i3.** Compd, compound.

| Compd | EC$_{50}$ (nM)[*] | | | | |
|---|---|---|---|---|---|
| | GH9 | p1579[†] | p5375[‡] | p1833[§] | p5735[¶] |
| **5e2** | 22.1 ± 6.88 | 14.8 ± 4.94 | 27.4 ± 7.59 | 20.5 ± 6.18 | 165 ± 37.6 |
| **5i3** | 11.1 ± 3.87 | 2.64 ± 0.67 | 12.5 ± 4.40 | 3.70 ± 0.67 | 18.3 ± 6.34 |
| ETR | 104 ± 38.2 | 74.9 ± 18.9 | 37.6 ± 8.06 | 11.1 ± 2.76 | 14.3 ± 5.07 |
| RPV | 1707 ± 339 | 1.26 ± 0.38 | 1.07 ± 0.30 | 1.31 ± 0.38 | 151 ± 32.0 |

[*]EC$_{50}$, concentration of compound that causes 50% inhibition of viral infection and determined in at least triplicate against HIV-1 virus in TZM-bl cell lines. [†]p1579, major NNRTI resistance mutation M230L, and accessory NNRTI resistance mutations E138G, H221Y, and F227L. [‡]p5375, major NNRTI resistance mutations K101E, E138K, and Y181C, and accessory NNRTI resistance mutation A98G. [§]p1833, major NNRTI resistance mutations K101E, Y181C, and G190A, and accessory NNRTI resistance mutation A98G. [¶]p5735, major NNRTI resistance mutations K101E and Y181V.

5i3$^{res}$ strain, V106I, V179D, and Y181C are usually primary mutations that directly cause drug resistance, while A98G and G333E are defined as secondary mutations that maintain RT function and improve viral fitness.

### Evaluation of phenotypic cross-resistance to selected HIV-1 strains

Resistance-associated mutations weaken the affinity for the target by affecting the interaction between the inhibitor and the binding pocket, thereby reducing the mutated virus' susceptibility to NNRTIs (11). Thus, 5e2 and 5i3 were evaluated for antiviral activity against HIV-1 IIIB, 5e2$^{res}$, and 5i3$^{res}$ strains, as well as for cytotoxicity in the MT-4 cell line. Meanwhile, a variety of antiretroviral drugs were assayed in parallel to assess cross-resistance against selected mutant strains, including the NNRTI drugs NVP, EFV, ETR, RPV, and DOR, and the NRTI drugs lamivudine (3TC), zalcitabine (ddC), didanosine (ddI), and zidovudine (AZT). The biological evaluation results, expressed as EC$_{50}$, CC$_{50}$, SI, and RF [resistance fold; EC$_{50(mutant\ strain)}$/EC$_{50(IIIB\ strain)}$ ratio], are summarized in tables S6 and S7.

As expected, both 5e2 and 5i3 suppressed the replication of HIV-1 IIIB very effectively at single-digit nanomolar levels (EC$_{50}$ = 4.5 and 1.4 nM). Of them, 5i3 was still shown to be the most potent HIV-1 IIIB inhibitor with an EC$_{50}$ value of 1.4 nM, similarly potent to some of the referenced antiretroviral drugs, and much more so than others (EC$_{50}$ = 0.0019 to 19.7 μM). Because the 5e2$^{res}$ and 5i3$^{res}$ strains demonstrated up to >3474-fold and 693-fold resistance to 5e2 and 5i3, respectively, the selected resistant strains led to sharply decreased antiviral potency compared to that against the IIIB strain. Nonetheless, 5i3 was endowed with moderate inhibitory activity toward 5e2$^{res}$ (EC$_{50}$ = 0.33 μM) and 5i3$^{res}$ (EC$_{50}$ = 0.98 μM) strains at submicromolar concentrations, which were comparable to those of EFV and ETR. However, 5e2 (EC$_{50}$ > 15.5 μM) and NVP were completely inactive against selected mutant strains.

Notably, no phenotypic cross-resistance was observed for all NRTI drugs toward 5e2$^{res}$ and 5i3$^{res}$ strains, with RF values ranging from 0.5 to 1.9. Among them, the most potent NRTI drug, AZT, exhibited equivalent antiviral activity against 5e2$^{res}$ (EC$_{50}$ = 0.0519 μM) and 5i3$^{res}$ (EC$_{50}$ = 0.0489 μM) strains as against the IIIB strain (EC$_{50}$ = 0.0409 μM), with RF values of 1.3 and 1.2, respectively. In addition, ddC (EC$_{50}$ = 0.69 μM and RF = 0.8) and ddI (EC$_{50}$ = 8.93 μM and RF = 0.5) were found to have similar and higher potency against 5e2$^{res}$ and 5i3$^{res}$ strains than against the IIIB strain (EC$_{50}$ = 0.89 and

19.7 μM), respectively. RPV had double-digit nanomolar inhibitory activity against 5e2$^{res}$ and 5i3$^{res}$ strains with EC$_{50}$ values of 16.6 and 74.6 nM, being far more potent than other NNRTI drugs. Intriguingly, 5e2 and 5i3 displayed remarkable activity against RPV-resistant strains (table S1 and Table 4), while RPV was also able to effectively inhibit the mutant strains selected by 5e2 and 5i3 (tables S6 and S7). In conclusion, our discovered NNRTI 5i3 and RPV share nonoverlapping resistance profiles, which may allow for combination use in HAART regimens to maximize the suppression of highly variable HIV strains.

### Structural basis for improved resistance profiles of lead compounds 5e2 and 5i3 against drug-resistant strains

To understand the basis for the resilience of 5e2 and 5i3 against drug-resistant strains, we determined co-crystal structures of WT RT and K101P/K103N/V108I (GH9) RT with 5e2 and 5i3 (no inhibitor density was detected in datasets collected from either GH9 RT co-crystals or soaks of RPV). The structures were solved by molecular replacement using the WT RT/RPV complex [Protein Data Bank (PDB) ID 4G1Q] (46) as the search template and were subsequently refined to between 1.99- and 2.36-Å resolution (table S8).

#### WT RT-NNRTI structures

Overall, the structures of WT RT with 5e2 and 5i3 were very similar to those of related RT complexes with K-5a2 and 25a (fig. S1A). Polder OMIT maps (47) for each ligand in either the WT RT or GH9 RT complexes are shown in Fig. 3. Figure 4 (A and B) depicts the main interactions of 5i3 and 5e2 with WT RT within the NNIBP and its three channels (tunnel, entrance, and groove). The left wing of both compounds is wedged into the tunnel through hydrophobic interactions with P95, Y181, Y188, F227, W229, and L234. The right wing of both compounds is bound into the groove by two hydrogen bonds with the main-chain carbonyl and amide of K101 and through hydrophobic contacts with L100, Y318, and P236. Additional hydrogen-bonding interactions are made at the roof of the NNIBP between 5i3 and V106 and between 5e2 and V106/K104 (Fig. 4, A and B).

As we reported previously (20, 48), the main difference in RT conformation between piperidine-substituted (K-5a2, 25a, and congeners) and DAPY NNRTIs (ETR and RPV) is the uplift of the loop connecting the β11 and β12 strands. Upon the binding of piperidine-substituted NNRTIs such as 5i3 and 5e2, the β11-β12 connecting loop of RT shifts upward ~7.4 Å compared to the RPV-bound structure. Similarly, P225 shifts outward ~3.5 Å to accommodate the
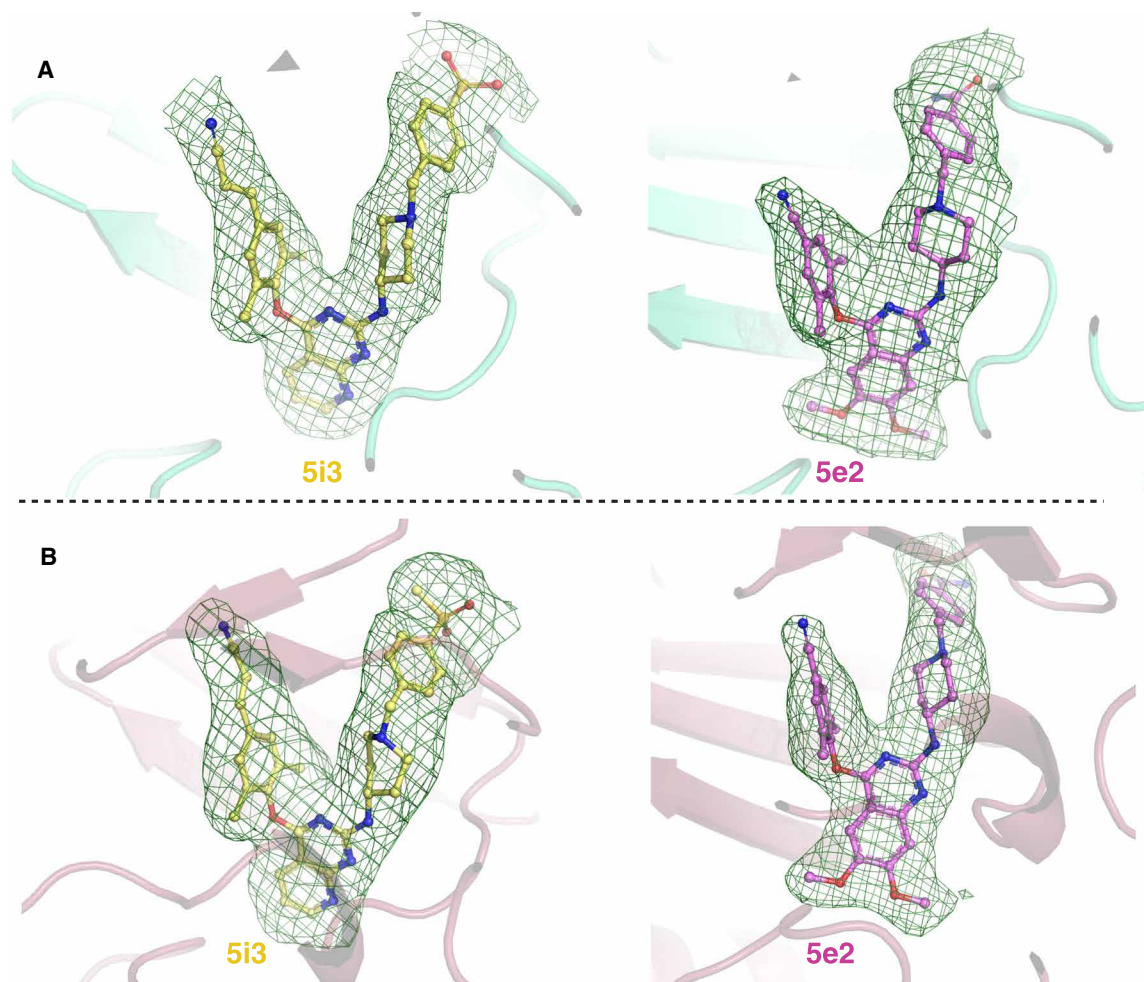
**Fig. 3. Polder OMIT maps for each ligand in either the WT RT or GH9 RT complexes.** (**A**) Polder OMIT maps for WT RT/**5i3** (1.99-Å resolution) and WT RT/**5e2** (2.18-Å resolution). (**B**) Polder OMIT maps for GH9 RT/**5i3** (2.36-Å resolution) and GH9 RT/**5e2** (2.15-Å resolution). All maps are shown at a contour of 3.0σ.

benzene-substituted group, which protrudes to the solvent-exposed surface of the enzyme (fig. S1B).

Regarding **5e2**, its extended central moiety fills the entrance channel and is engaged by hydrophobic and polar contacts with E138 of the p51 subunit, L100 (hydrophobic contacts), and K101 (hydrogen bonding with the main-chain amide nitrogen). The side chain of K101 moves away from the entrance channel to accommodate the methoxy substituents (fig. S1, C and D). Regarding **5i3**, its central moiety is likewise in extensive contact with E138 of p51 (via hydrophobic contacts). Moreover, the presence of a nitrogen atom on the terminal six-membered ring (absent in **5e2**) enables a water-mediated hydrogen bond with the side chain of K103 (fig. S2) that could explain the improved potency of **5i3**.

### GH9 mutant RT-NNRTI structures and basis for improved resistance profiles of lead compounds 5e2 and 5i3 against drug-resistant strains

In both GH9 RT complexes (Fig. 4, C and D, and fig. S3), the ligand shifts relative to the WT structures: **5e2** shifts downward ~0.8 Å, and **5i3** shifts upward ~0.8 Å. This may be related to the inability of P101 to act as a hydrogen bond donor via its main-chain nitrogen. In the

**5e2** structure, the amino group of N103 participates in hydrogen-bonding interactions with the ligand. For **5i3**, the main-chain carbonyl group of P101 provides the hydrogen bond that in the WT complexes is done with the main-chain carbonyl of K101. In contrast, the amino group of the side chain of N103 provides the hydrogen bond that in the WT complexes is established with the main-chain carbonyl of K101 (Fig. 4, C and D). Overall, the conformational flexibility of the piperidine-substituted phenyl groups on the right wing enables comparable interactions within the WT and GH9 complexes.

The mutation of V108I provokes a reconfiguration of some NNIBP residues, forming the tunnel channel where the left wing of **5e2** and **5i3** is binding. Nevertheless, both ligands yield different rearrangements in each complex. In the GH9 RT/**5e2** complex, the side chain of V108I protrudes toward the benzonitrile substituent, and the F227 side chain rotates 90° to avoid clashing with the former. The more distant F227 is displaced ~3 Å from Y188, which is shifted ~1 Å away from its position in the WT complex (Fig. 5A). The Y183 phenoxyl ring in GH9 RT is displaced up to 4 Å away from its position in WT RT.
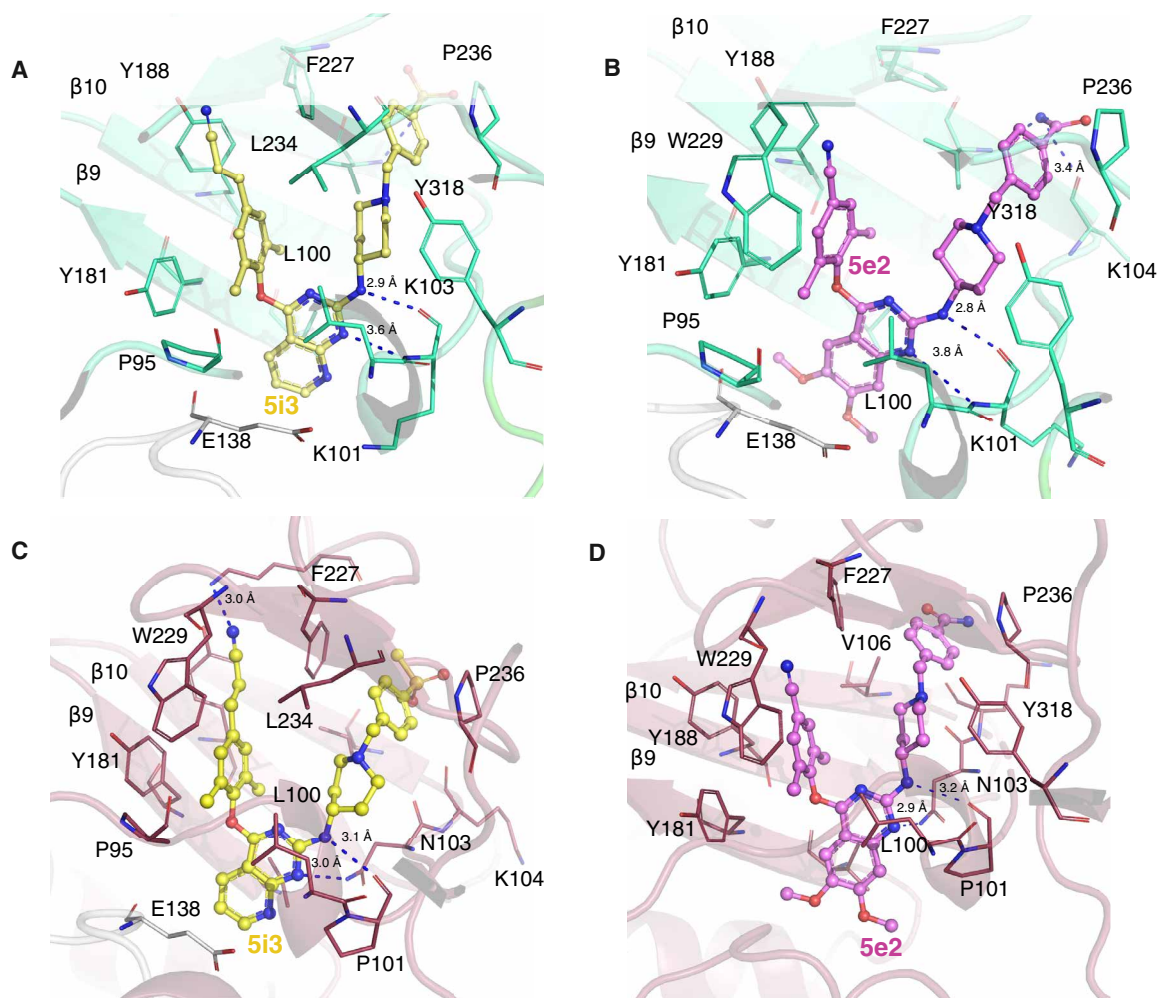
**Fig. 4. Interactions of WT RT and GH9 RT with bound inhibitors.** (**A**) Co-crystal structures of **5i3** (yellow ball and stick) and WT RT (green sticks). (**B**) Co-crystal structures of **5e2** (violet ball and stick) and WT RT (green sticks). (**C**) Co-crystal structures of **5i3** (yellow ball and stick) and GH9 RT (red sticks). (**D**) Co-crystal structures of **5e2** (violet ball and stick) and GH9 RT (red sticks). Hydrogen bonds are indicated by blue lines and waters are shown as red spheres.

On the other hand, in the GH9 RT/**5i3** complex, the bulkier V108I residue interacts with the K223 side chain, restricting its movement (Fig. 5B and fig. S4). This is afforded by a shift downward of the β12 strand, which may be provoked by a rearrangement of the hydrogen-bonding network in the right wing of **5i3**. In practice, this allows the remaining portion of the tunnel channel to maintain a conformation like that of the WT complex. Additionally, K223 establishes additional stabilizing interactions with both the nitrogen of the cyanovinyl group in **5i3** and the hydroxyl substituent in Y188 (Fig. 5B).

While the structures with WT/GH9 RT with **5e2** and **5i3** explain their resilience against the RPV-resistance mutations, they do not directly explain the reason for the inhibition drop of RPV with GH9 RT. Nevertheless, we have performed a comparative structural analysis, including the WT RT/RPV complex (PDB ID 4G1Q) (*46*). We have detailed that the piperidine-aryl–substituted NNRTIs' longer right wing causes uplift of the "primer grip" region comprising the β12-β13-β14 sheet, including key residues P225 and P236 (fig. S1B). While RPV is effective against K103N RT, the IC$_{50}$ for RPV against K101P RT increases 20-fold relative to WT RT (*20*). Nevertheless, RPV's right wing, with its smaller cyano-aryl ring rather than the

larger piperidine-aryl–substituted moiety, does not fully open the groove channel, providing a more constrained NNIBP "roof" (figs. S1B and S5).

As shown above, the complexes with **5e2** and **5i3** exhibit two distinct rearrangements of nearby residues, which appear to compensate for the bulkier V108I mutation in the tunnel region of the GH9 mutant. Moreover, these rearrangements effectively compensate for changes in the hydrogen-bonding network of the groove channel, as evidenced by the shifting NNIBP residues in the right wing (fig. S1B). As a result, the expanded roof region of the NNIBP, attributed to the longer right-wing piperidine-aryl–substituted **5e2** and **5i3**, allows them to "wiggle and jiggle" more efficiently when compared to RPV-bound structures. The increased number of rotatable bonds also contributes to their more efficient conformational flexibility and positional adaptability, thus resilience against RPV resistance mutations (fig. S5).

Furthermore, we have performed molecular docking of RPV to "GH9 RT" (receptor GH9 RT of GH9 RT/**5e2**) with **5e2** and **5i3**, as well as with "WT RT" (receptor RT from PDB ID 4G1Q) and the "in silico GH9 RT" (receptor made from in silico mutation of RT
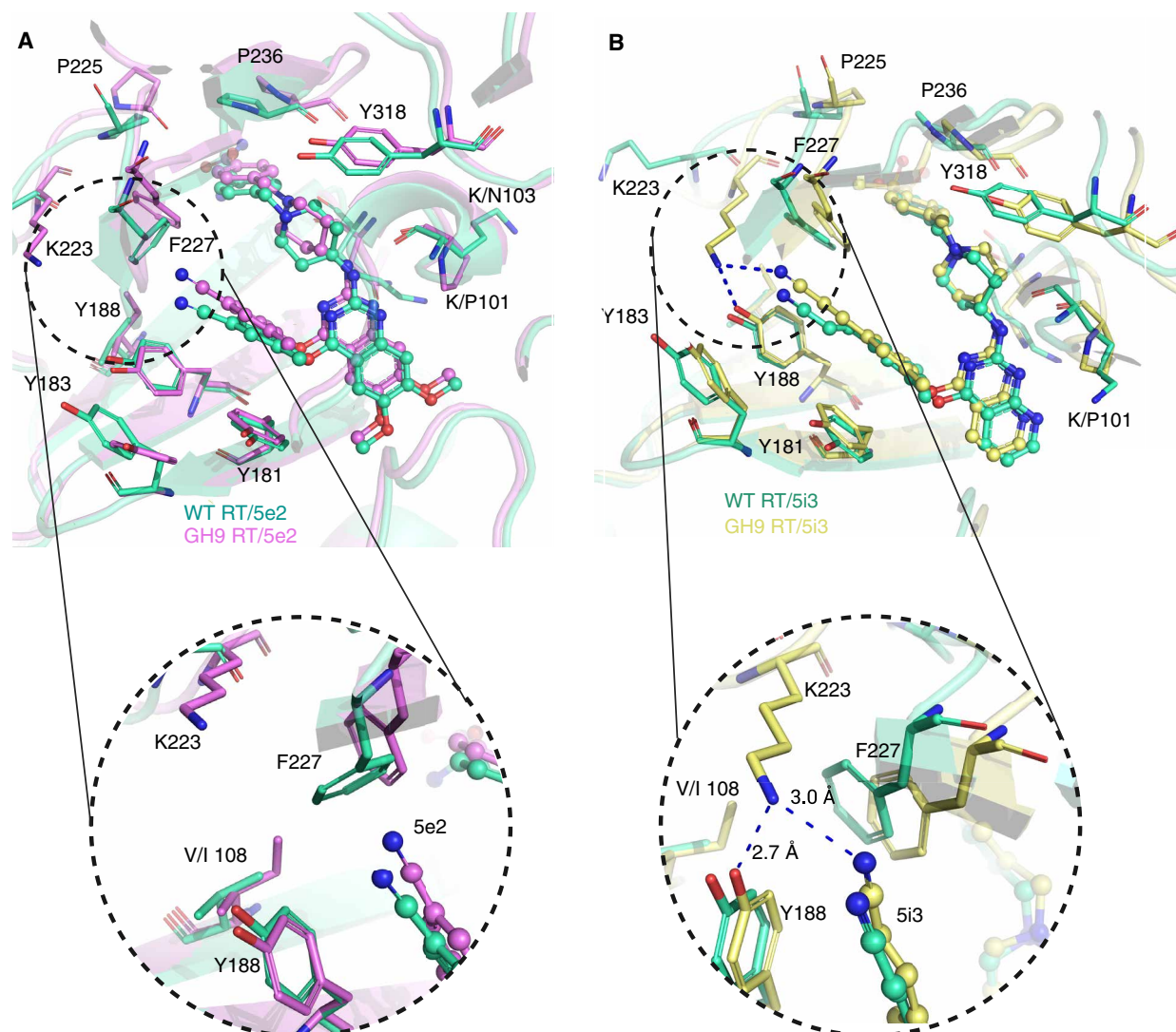
**Fig. 5. Superposition of WT and K101P/K103N/V108I (GH9) RT complexes illustrate rearrangements of the NNIBP to overcome resistance mutations.** (**A**) WT RT bound to **5e2** (pale green) superposed onto GH9 RT bound to **5e2** (violet). (**B**) WT RT bound to **5i3** (pale green) superposed onto GH9 RT bound to **5i3** (pale yellow). Zoomed-in regions are shown at the bottom of the image. Hydrogen bonds are shown as blue sticks, and hydrophobic interactions are shown as yellow dashes.

in PDB ID 4G1Q). The latter provides the controls and benchmark for supporting the extracted SAR (see Materials and Methods for detail). Using the GH9 RT/**5e2** receptor, redocking of **5e2** and docking of **5i3** provide similar ligand poses (fig. S6, A and B) and good scoring, similar to the scoring of redocking RPV to WT RT/RPV receptor (fig. S6C). Docking of RPV with the in silico GH9 RT receptor is not compatible with binding to the NNIBP, RPV is placed away from it (fig. S6D), while docking with the GH9 RT/**5e2** receptor provided a worse score than with **5e2** or **5i3** (fig. S6E). Additionally, no previous structure of WT or mutant RT in complex with RPV shows an enlarged groove channel unlike any of the inhibitors presenting an extended right wing (K-5a2, 25a, **5e2**, and **5i3**). In conclusion, molecular docking corroborates that the arrangement of RPV in GH9 RT must be very unfavorable, explaining the poor inhibition of the GH9 strain by RPV.

## CYP enzymatic inhibitory assay

The key metabolic enzymes cytochrome P450 (CYP450) in the liver are widely involved in most drug metabolism processes in vivo, especially the major subtypes of the CYP450 superfamily: CYP2C9, CYP2C19, CYP2D6, and CYP3A4. Potent inhibition of CYP enzymes by certain drugs can alter the metabolic pathways of other coadministered drugs, which may induce adverse drug-to-drug interaction (DDI) or even treatment failure (*49*, *50*). However, in vivo metabolic studies have shown that combining ETR and RPV with other antiretroviral drugs can cause metabolism-mediated DDIs due to their potent inhibition of CYP2C9 and CYP2C19 isozymes (*51*).

Consequently, **5i3** was investigated for its ability to inhibit five main subtypes, including CYP1A2, CYP2C9, CYP2C19, CYP2D6, and CYP3A4. ETR and RPV were selected as the reference drugs, and standard inhibitors of these enzymes were used as positive

controls. As shown in table S9, **5i3** showed only faint inhibition of CYP1A2 ($IC_{50}$ = 56.6 μM), CYP2C9 ($IC_{50}$ = 6.76 μM), CYP2C19 ($IC_{50}$ = 8.47 μM), and CYP2D6 ($IC_{50}$ = 12.7 μM), at levels which were generally lower than those of standard inhibitors ($IC_{50}$ = 0.134 to 0.512 μM), ETR ($IC_{50}$ = 0.277 to 12.04 μM), and RPV ($IC_{50}$ = 0.335 to 9.11 μM). As for the CYP2C9 and CYP2C19 subtypes inhibited by ETR and RPV, **5i3** had reduced inhibitory potency of 6.76 and 8.47 μM, being 17- to 25-fold lower than ETR ($IC_{50}$ = 0.277 and 0.496 μM) and RPV ($IC_{50}$ = 0.346 and 0.335 μM). Regarding CYP3A4, the most clinically important CYP isoform, **5i3** ($IC_{50}$ = 5.86 μM), showed a 2.7-fold improvement over RPV ($IC_{50}$ = 2.17 μM) in CYP3A4 inhibition but was still inferior to that of ETR ($IC_{50}$ = 41.3 μM). The results demonstrated that **5i3** had substantially improved CYP inhibition profiles over ETR and RPV, except for the CYP3A4 subtype, suggesting a reduced DDI effect in the combined regimen.

### hERG inhibitory activity assessment

The hERG encodes the pore-forming potassium channel subunit that mediates rapidly activating delayed rectifier $K^+$ current ($I_{Kr}$). Off-target binding of non-cardiovascular drugs to the hERG potassium channel could potentially prolong the duration of ventricular action, leading to the acquired long QT syndrome with mortality risk from cardiac arrest ([38, 52]).

To assess the hERG-related cardiotoxicity, the hERG potassium channel inhibition assay of **5i3** was performed in Chinese hamster ovary (CHO) cells transfected with hERG cDNA using the electrophysiological manual patch-clamp technique, with RPV as the reference drug ([53]). As depicted in tables S10 and S11, the hERG channel inhibition rate of **5i3** was slightly decreased compared to that of RPV at the same tested concentrations. **5i3** and RPV displayed hERG inhibitory activity with $IC_{50}$ values of 1.48 and 1.21 μM, respectively (Fig. 6A and fig. S7). Nevertheless, the $IC_{50}$ value of **5i3** translates into a reduced hERG liability compared to that for K-5a2 ($IC_{50}$ = 0.13 μM) and 25a ($IC_{50}$ = 0.18 μM). Therefore, **5i3** had a slightly improved hERG-related cardiac safety profile over our previous leads, and comparable to RPV.

### In vivo acute toxicity assessment

A single-dose acute toxicity assay of **5i3** was conducted in healthy Kunming mice. After oral administration of **5i3** at a dose of 800 mg/kg, no mortality occurred, and no abnormal behaviors (i.e., anorexia, lethargy, fur folds, and chronic convulsions) were observed compared to the blank control group. All mice in the administered group grew normally, as did the control group. As shown in Fig. 6B, all mice gradually gained weight over a period of 7 days. Thus, **5i3** was well tolerated at a dose of 800 mg/kg with no acute toxicity in mice.
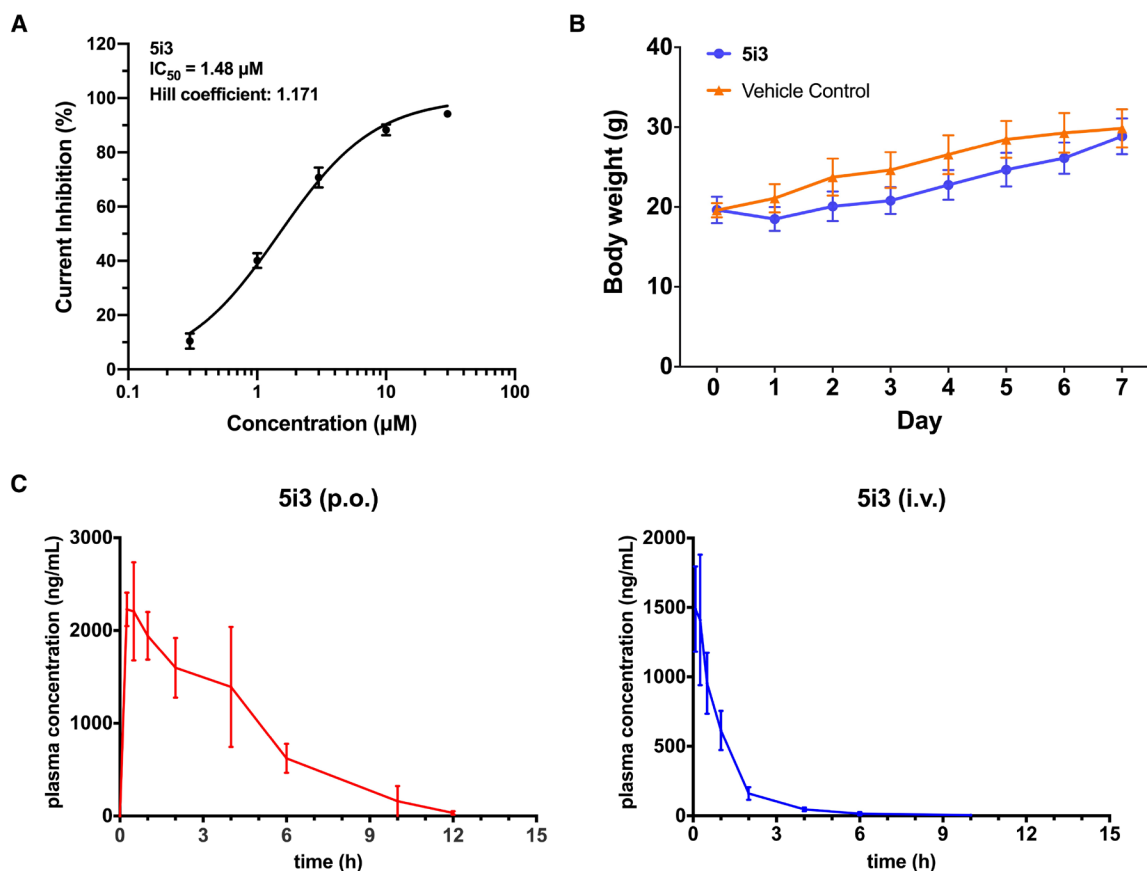


**Fig. 6. Preliminary drug-like profiles evaluation of compound 5i3.** (**A**) Inhibitory activity of compound **5i3** against the hERG potassium channel in the CHO-hERG cell. (**B**) Body weights of all Kunming mice in the **5i3** administration group and the vehicle control group during the acute toxicity assay. (**C**) Plasma concentration–time curve of **5i3** following oral administration (20 mg/kg po) and intravenous administration (2 mg/kg iv) in Sprague-Dawley rats.

## In vivo PK study

The efficacy of antiviral agents depends not only on the inhibitory activity in vitro but also on the PK profiles in vivo (54, 55). Encouraged by the high potency and low toxicity, the PK profiles of **5i3** and ETR were further evaluated in Sprague-Dawley rats by single intravenous and oral administration (tables S12 and S13). Figure 6C and fig. S8 show the plasma concentration–time curves of **5i3** and ETR after a single dose was administered [of 2 mg/kg intravenously (iv) and 20 mg/kg orally (po)]. After intravenous administration, the plasma concentration began to decrease from $T_0$ (time zero). Meanwhile, after oral administration, the plasma concentration increased to $T_{max}$ (time of maximum plasma concentration) and then decreased slowly, indicating that **5i3** was rapidly absorbed into plasma and then slowly eliminated by in vivo metabolism. Specifically, when administered intravenously, **5i3** was characterized by a moderate clearance rate (CL = 20.6 ml/min per kilogram) and half-life ($T_{1/2}$ = 1.59 hours). The absorption of **5i3** after oral administration reached a maximum concentration ($C_{max}$) of 2354 ng/ml at 0.417 hours ($T_{max}$) with an oral half-life of 1.77 hours. In addition, the area under the plasma concentration–time curve ($AUC_{0-inf}$) and mean residence time ($MRT_{0-inf}$) for **5i3** were 10033 ng·hour/ml and 3.48 hours, which were superior to those of ETR ($AUC_{0-inf}$ = 421 ng·hour/ml; $MRT_{0-inf}$ = 3.03 hours). Notably, the oral bioavailability (*F*) of **5i3** was as high as 59.9%, substantially higher than that of ETR (*F* = 7.17%) and sufficient to support the potential of **5i3** as an orally bioavailable NNRTI drug candidate. Nonetheless, the current relatively short half-life of **5i3** may pose a potential limitation to once-daily dosing, and we will subsequently explore further optimization approaches, such as formulation strategies or structural modifications, to achieve sustained drug exposure suitable for once-daily dosing.

## DISCUSSION

HIV-1 NNRTIs are an essential component of HAART regimens; however, concerns regarding cross-resistance and safety continue to pose challenges to their clinical use. The emergence of clinically resistant strains results in greatly reduced susceptibility to NNRTIs. Cross-resistance evaluation showed that the triple-mutant strain K101P/K103N/V108I (GH9) confers >162- and 18-fold resistance to RPV and ETR, respectively, which can markedly reduce their clinical efficacy. Therefore, in the current landscape of antivirals options, there remains an urgent demand for the NNRTI with enhanced resilience and tolerance to improve the long-term treatment potential of regimens containing NNRTIs.

Along these lines, the first long-acting regimen for HIV treatment, Cabenuva (cabotegravir, an integrase strand transfer inhibitor, plus RPV), was approved by the European Medicines Agency (EMA) in 2020 and the FDA in 2021 (56). Access to long-acting Cabenuva by marginalized patient populations could enable considerable progress toward treatment adherence and reaching the Joint United Nations Programme on HIV/AIDS (UNAIDS) 2030 95-95-95 goal (calling for 95% of people living with HIV to know their status, 95% of all people diagnosed with HIV infection to be receiving antiretroviral therapy, and 95% of patients receiving antiretroviral therapy) (56). A recent in-depth case analysis of virological failure in multiple people with HIV receiving Cabenuva was associated with NNRTI-resistance mutations, highlighting again the hazards of drug resistance in HIV treatment (57).

Herein, informed by our efforts in optimizing DAPY-type NNRTIs and their co-crystal structures, we designed and synthesized a series of DAPY-evolved derivatives by further exploring the chemical space that can be accommodated in the RT NNIBP. Preliminary SAR were investigated through three rounds of structural modifications, providing valuable insights for molecular elaboration. The biological activity results showed that all compounds exhibited robust potency at inhibiting WT HIV-1 strain replication in the low nanomolar ranges. Among them, the pyrido[2,3-*d*]pyrimidine derivative **5i3** and 6,7-dimethoxyquinazoline derivative **5e2** yielded remarkable activity against the WT strain with an $EC_{50}$ value of 1.16 nM, which was comparable to ETR ($EC_{50}$ = 1.42 nM). **5i3** ($EC_{50}$ = 11.1 nM) and **5e2** ($EC_{50}$ = 22.1 nM) were found to be exceptionally effective against the GH9 strain, being far more potent than RPV ($EC_{50}$ = 1707 nM) and other NNRTI drugs. In addition, **5i3** showed potent inhibition against HIV-1 viral isolates carrying multiple NNRTI-resistance mutations ($EC_{50}$ = 2.64 to 18.3 nM), with generally about 3 to 28 times more activity than those of ETR ($EC_{50}$ = 11.1 to 74.9 nM) or RPV ($EC_{50}$ = 1.07 to 151 nM). We did not investigate the activities of **5i3** and **5e2** against strains with single NNRTI-resistant mutations. No overlapping drug resistance profiles were observed between **5i3** and RPV, supporting future potential NNRTI-based combination antiretroviral therapies.

An HIV-1 WT strain (IIIB) was cultured in MT-4 cells for 39 passages under drug-selective pressure to investigate the kinetics of emerging resistance to **5i3** and **5e2**. Resistance-associated mutations in the RT gene of selected mutant strains were further determined in comparison to the DNA sequences of the WT strain, including the L100I, V179D, and Y181C mutations for the **5e2**[res] strain, and the A98G, V106I, V179D, Y181C, and G333E mutations for the **5i3**[res] strain. No phenotypic cross-resistance was observed for RPV and NRTI drugs toward the **5e2**[res] and **5i3**[res] strains. The antiviral activities of the most potent NRTI drug, AZT, against the **5e2**[res] ($EC_{50}$ = 0.0519 μM) and **5i3**[res] ($EC_{50}$ = 0.0489 μM) strains were comparable to those against the IIIB strain ($EC_{50}$ = 0.0409 μM).

Structural biology has implications for understanding the molecular mechanisms of drug resistance and assisting in drug design. Our crystallographic studies revealed the structural basis for the resilience to the GH9 strain, with the bulky piperidinyl of **5i3** and **5e2**, leading to pocket expansion and structural rearrangement of NNIBP, providing greater space for modifications to adapt to distinct pocket architecture and enabling efficient binding in mutant RTs. Additionally, **5i3** and **5e2** have a higher number of rotatable bonds (with 8 and 9, respectively) than RPV, DOR (both with 5), and earlier NNRTIs [fig. S5 and reviewed in (58)]. The number of rotatable bonds of an NNRTI shows a notable correlation with drug efficacy for RT mutant strains. Hence, **5i3** and **5e2** are evolved DAPYs that exhibit a conformational "roof-raising" effect on the NNIBP, enabling additional modes of conformational flexibility and positional adaptability. These characteristics correlate with their exceptional resilience to drug resistance, further highlighting the efficacy of this drug design concept (59). Our crystallographic studies have thus provided experimental evidence of this concept in action, dealing with the challenging mutant GH9 RT.

A high-quality drug should have a finely tuned combination of effective bioactivity, suitable physicochemical properties, and favorable safety profiles. Preliminary drug-likeness evaluation showed that **5i3** not only displayed reduced CYP inhibition ($IC_{50}$ = 5.86 to 56.6 μM) and hERG inhibition ($IC_{50}$ = 1.48 μM) but also exhibited

a favorable in vivo safety profile ($LD_{50}$ > 800 mg/kg). Furthermore, **5i3** had appealing in vivo PK properties, characterized by a moderate half-life ($T_{1/2}$ = 1.77 hours) and excellent oral bioavailability ($F$ = 59.9%).

In the current work, we rationally designed a series of DAPY-evolved derivatives as potent HIV-1 inhibitors to explore the RT allosteric pocket using a structure-based drug design strategy. The biological evaluation results showed that the most potent pyrido[2,3-*d*]pyrimidine derivative **5i3** was endowed with broad-spectrum antiviral activities and higher resistance profiles against a panel of multiple NNRTI-resistant strains compared to ETR and RPV. In particular, **5i3** proved to be an effective inhibitor against one of the most RPV-resistant triple-mutant strains GH9. No overlapping drug resistance profiles were observed between **5i3** and RPV or NRTI drugs, supporting synergistic use to maximize suppression of clinically mutant strains in the NNRTI-based combination regimen. Furthermore, **5i3** had favorable drug-like properties characterized by excellent safety and in vivo PK profiles. Given the recent emphasis on long-acting drugs in therapy, we want to explore whether a long-acting formulation of **5i3** is feasible and whether it helps to improve the clearance half-life. Together, our discovered compound **5i3**, characterized by its efficiency, low toxicity, and favorable drug-like properties, exhibits substantial potential as a promising drug candidate for HIV therapy.

## MATERIALS AND METHODS

### Statistics

All statistical data are presented as the means ± SD. The indicated sample size (*n*) represents biological replicates. All biological evaluation and animal experiments were performed in at least triplicates, with average values and SD calculated accordingly. For crystal structures, 95 to 100% complete datasets were collected and used (table S8). A random set of 5% data was used as R-free (also known as free residual factor) set in the refinement of each crystal structure to avoid model bias. The final sample size was determined when the quality of the density maps was clearly resolved for side chains and the R-free value for each crystal structure reached the lowest values. X-ray datasets contained large sample sizes with final maps clearly resolving side chain density, and, therefore, as a standard practice, no replication of structure determination is required.

### In vitro anti-HIV assay in TZM-bl cells

Anti–HIV-1 activity of NNRTIs was measured as reductions in a *Luc* reporter gene expression system after virus infection of TZM-bl cells (*60*). HIV-1 virus (NL4-3, GH9, p1579, p5375, p1833, and p5735) at 200 median tissue culture infectious dose, various dilutions of test samples (eight dilutions, fourfold stepwise), and TZM-bl cells ($10^4$ cells) were mixed in a total volume of 150 μl of growth medium in each well of 96-well black solid plates (Corning-Costar). One set of eight control wells received cells plus virus (virus control), and another set of eight wells received cells only (background control). After 48 hours of incubation, the culture medium was removed from each well, and 100 μl of Promega Bright-Glo Luciferase Assay reagent was added to the cells. After 2 min of incubation at room temperature, the luciferase activity in the assay wells was measured using a Perkin-Elmer Victor X luminometer. The $EC_{50}$ was defined as the sample concentration that caused a 50% reduction in

relative luminescence units (RLU) compared to virus control wells after subtraction of background RLU.

The cytotoxicity of NNRTIs was determined using a colorimetric 2,3-bis-(2-methoxy-4-nitro-5-sulfophenyl)-2*H*-tetrazolium-5-carboxanilide (XTT) assay (*61*, *62*). Test samples (100 μl) at graded concentrations were added to equal volumes of 96-well plates inoculated with TZM-bl cells ($5 \times 10^5$/ml). After 4 days of incubation at 37°C, the 50 μl of XTT solution (1 mg/ml) containing 0.02 μM phenazine methosulfate was added to the 96-well plate. After 4 hours of incubation, the absorbance value at 450 nm was measured using an enzyme-linked immunosorbent assay reader. The $CC_{50}$ was defined as the sample concentration that caused a 50% reduction in cell viability.

### In vitro selection of HIV-1 (IIIB) mutant strains

HIV-1 strains resistant to **5e2** and **5i3** were obtained after sequential passaging of HIV-1 (IIIB) in the presence of increasing concentrations of **5e2** and **5i3** in MT-4 cells (*63*). At the start of the selection, MT-4 cells were inoculated with HIV-1 (IIIB) in the presence of a 6.2 nM concentration of **5e2** and 4.4 nM concentration of **5i3**. The cultures were passaged every 3 to 4 days. When a cytopathogenic effect (CPE) was observed, the cell culture supernatant was used as an inoculum to infect new MT-4 cells at the same compound concentration. The concentration of the compound was increased after the second observation of CPE. After serial passaging (39 passages), we were able to culture the resistant virus in the presence of 8.8 and 5.3 μM of **5e2** and **5i3**, respectively. In a parallel control experiment, HIV-1 (IIIB) was cultured in MT-4 cells without any compound.

### Genotypic evaluation

RNA was extracted from virus stock using the QIAamp Viral RNA mini Kit (QIAGEN, Venlo, The Netherlands) as described in the manufacturer's protocol. The procedures for the preparation of samples for RT-PCR amplification and sequencing have been reported elsewhere (*64*, *65*). Genotypic analysis was performed after 13, 25, and 39 passages.

### Evaluation of phenotypic cross-resistance to selected resistant strains

The anti-HIV activity and cytotoxicity of **5e2**, **5i3**, and antiretroviral drugs were evaluated using the 3-(4,5-dimethylthiazol-2-yl)-2,5-diphenyltetrazolium bromide (MTT) assay in MT-4 cells as described previously (*66*, *67*). The MTT assay is based on the HIV-induced CPE and measures the degree of cell killing on HIV infection.

First, 25-μl volumes of the test sample stock solution were added to triplicate wells of two parallel assays on the 96-well plates to simultaneously determine their effects on mock- and HIV-infected MT-4 cells. Then, 100 μl of medium was added to 25 μl of stock solution via the Biomek 3000 robot (Beckman Instruments, Fullerton, CA), and 25 μl of this solution was transferred to another well that contained 100 μl of medium to prepare serial fivefold dilutions of test compounds on the 96-well plates. The HIV-1 WT strain (IIIB) and selected resistant strains **5e2**[res] and **5i3**[res] stock (50 μl) at 100 to 300 $CCID_{50}$ (50% cell culture infectious dose) or culture medium and MT-4 cell culture solution (50 μl) were further added to the 96-well plates. After 5 days of incubation at 37°C and 5% $CO_2$, 20 μl of MTT solution was added to each well and incubated for an additional 2 hours. The wells were centrifuged at 1000 rpm for 5 min, and the supernatant was discarded. Dimethyl sulfoxide (DMSO)

was added to the wells to dissolve the deposited formazan fully, and the absorbance of each well was read in an eight-channel computer-controlled photometer (Infinite M1000, Tecan) at two wavelengths (540 and 690 nm). All data were calculated using the median absorbance value of three wells. The $EC_{50}$ was defined as the concentration of the test compound that achieved 50% protection from the cytopathic effect of HIV in infected MT-4 cells. The $CC_{50}$ was defined as the concentration of the test compound that reduced the viability of the mock-infected MT-4 cells by 50%.

### Cloning and protein preparation

RT52A, an engineered HIV-1 RT construct optimized for RT-NNRTI co-crystallization (68), was used as the template for site-directed mutagenesis to introduce the three mutations K101P, K103N, and V108I in the p66 subunit. RT52A, referred to as WT RT, and K101P/K103N/V108I RT52A, referred to as GH9 RT, were expressed and purified as described previously (18, 68).

### Crystallization

For WT and GH9 RT, the crystallization procedure was carried out analogously, with the following exceptions. WT/GH9 RT (20 mg/ml) was incubated with **5e2**, **5i3**, and RPV [the last just for GH9 RT, as the WT RT/RPV was previously solved by the Arnold lab (46), PDB ID 4G1Q] at a 1:1.5 protein/drug molar ratio at room temperature for 30 min, except for RPV, incubated at a 1:117 ratio. Co-crystals of RT with **5e2**, **5i3**, and RPV were set up in hanging drops at 4°C with a 1:1 ratio of the protein-ligand complex and reservoir [10% (v/v) poly(ethylene glycol) (PEG)–8000, 4% (v/v) PEG-400, 100 mM MES (pH 6.3), 10 mM spermine, 15 mM $MgSO_4$, 100 mM ammonium sulfate, and 5 mM tris(2-carboxyethyl)phosphine] together with an experimentally optimized concentration of microseeds made by crushing previously obtained RT/RPV crystals (pre-seeding). The crystals were cryo-protected by dipping them into the reservoir with 25% ethylene glycol and plunge-frozen in liquid $N_2$. X-ray data were collected from three of the plunge-frozen crystals at the APS 23-ID-D and CHESS ID7B2 beamlines. The crystallographic software packages HKL2000 (69), Phenix (70), and Coot (71) were used for data processing, structure refinement, and model building, respectively. **5e2** and **5i3** coordinates and restraints were generated using the Grade Web Server (http://grade.globalphasing.org). The structure was solved by molecular replacement using PDB ID 4G1Q as the template. The diffraction data and refinement statistics are summarized in table S8.

### Structural analysis and docking

Manual superposition and evaluation of WT and resistant mutant RT structures with NNRTIs were performed with Coot (71). The Proteins*Plus* web server (72) was used to run molecular docking with JAMDA (73). Pocket volumes were calculated with PyVOL (74), and the number of rotatable bonds of NNRTIs was assessed with the SwissADME web tool (75).

### Cytochrome P450 inhibition assay

Compound **5i3** was incubated with human liver microsomes and reduced form of nicotinamide adenine dinucleotide phosphate (NADPH) cofactor in the presence of CYP1A2 substrate phenacetin, CYP2C9 substrate diclofenac, CYP2C19 substrate *S*-mephenytoin, CYP2D6 substrate dextromethorphan, and CYP3A4 substrate midazolam, respectively. Standard CYP enzyme inhibitors were screened

alongside **5i3** as positive controls. Working solutions of experimental and control compounds were prepared at 100× concentration. The substrate solutions (20 μl) were added to corresponding wells, and then 20 μl of potassium phosphate buffer was added to blank wells. Either the test compound or positive control working solution (2 μl) was added to corresponding wells. Subsequently, 2 μl of solvent was added to wells containing no inhibitor, and 2 μl of potassium phosphate buffer was added to blank wells. Human liver microsomes (0.114 ml) were added to 8.886 ml of potassium phosphate buffer to prepare the microsome working solution (0.253 mg/ml). Next, 158 μl of the HLM working solution was added to all wells of the incubation plate. The plate was preincubated for 10 min in a 37°C water bath. NADPH cofactor (62 mg) was added to 6.0 ml of $MgCl_2$ buffer to prepare the NADPH solution (10 mM). The NADPH solution (10 mM; 20 μl) was then added to all incubation wells. The plate was incubated for 10 min in a 37°C water bath. Reactions were terminated at specified time points by adding 400 μl of cold stop solution (tolbutamide at 200 ng/ml and labetalol at 200 ng/ml in acetonitrile). The samples were centrifuged at 4000 rpm for 20 min to precipitate the protein. Supernatant was (200 μl) diluted with 100 μl of water and left to shake for 10 min. Last, the samples were sent for liquid chromatography–tandem mass spectrometry (LC-MS/MS) analysis.

### hERG channel inhibition assay

The hERG channel inhibition of compound **5i3** and RPV was determined in CHO cells stably transfected with hERG cDNA. CHO-hERG cells expressing hERG were plated in F12 dishes for 24 hours and maintained at 37°C under 5% $CO_2$. A micropipette was drawn out from the borosilicate glass to give a tip resistance between 2 and ~5 megohms. For each trial, a single dish of cells was removed from the incubator, washed twice with extracellular solution (ECS), and placed on the microscope. CHO-hERG cells in the exponential growth phase were collected and resuspended in ECS for later use. The whole-cell recordings were conducted with a commercially available patch-clamp amplifier. The CHO-hERG cells were placed on the microscope stage, and one cell in the recording tank was randomly selected for testing. The perfusion system was fixed on an inverted microscope stage, and the cells were continuously perfused with ECS. Tail currents were evoked once every 15 s by a 1275-ms, −50-mV repolarizing pulse following an 850-ms, +60-mV depolarizing pulse with a hold voltage of −80 mV. The voltage protocol started with a 50-ms depolarization pulse of −50 mV, which served as the baseline for calculating the peak tail current amplitude. Only stable cells with recording parameters exceeding the threshold were used in the experiments. The hERG currents were allowed to stabilize over a 3-min period in the presence of vehicle alone before the test compound application. The cells were kept in the test solution until the peak tail current was stable (<5% change) for about three sweeps. Peak tail amplitudes were then plotted as a function of the sweep number. Before testing the composite application, the average of the three peak tail currents in the steady state was taken as the control current amplitude. Four or five peak tail current measurements at the steady state after the test compound application were averaged and used as the remaining current amplitude after inhibition by the test compound. hERG inhibition rate was calculated by the following formula: Inhibition % = [1 − (remaining current amplitude)/(control current amplitude)] × 100%.

## In vivo acute toxicity assessment

All animal treatments were performed strictly in accordance with the institutional guidelines of animal ethics and welfare after gaining approval from the Medical Ethical Committee of Shandong University (no. 19008). Twelve Kunming mice (17 to 22 g) were randomly divided into two groups to receive compound **5i3** or vehicle solution. Compound **5i3** was suspended in a mixture solution of PEG-400 and normal saline. All mice were fasted for 12 hours. Mice in the test group were administered a single dose of **5i3** (800 mg/kg) intragastrically on the first day. In contrast, mice in the control group were administered with the same volume of vehicle solution. The death, abnormal behaviors, and body weight of these mice were monitored every day during the subsequent seven days.

## In vivo PK assay

All animal treatments were performed strictly in accordance with the institutional guidelines of animal ethics and welfare, after gaining approval from the Medical Ethical Committee of Shandong University (no. 19008). Six Sprague-Dawley rats (220 to 240 g) were randomly divided into two groups to receive oral administration (20 mg/kg) or intravenous administration (2 mg/kg). Compound **5i3** was prepared as a clear solution of 0.40 mg/ml in 3% DMSO, 60% PEG, and 37% water for intravenous administration and 2.00 mg/ml in 3% DMSO, 60% PEG, and 37% water for oral administration, respectively. Blood samples (200 μl of blood each time) of the intravenous group were collected from the sinus jugular into heparinized centrifugation tubes at 5 min, 15 min, 30 min, 1 hour, 2 hours, 4 hours, 6 hours, and 10 hours after dosing. The oral administration group samples (200 μl of blood each time) were collected at 15 min, 30 min, 1 hour, 2 hours, 4 hours, 6 hours, 10 hours, and 12 hours after dosing. All the plasma samples were obtained by centrifugation at 8000 rpm for 8 min and immediately stored at −80°C until analysis. LC-MS/MS analysis was used to determine the concentration of **5i3** in plasma. Briefly, 50 μl of plasma was added to 50 μl of internal standard and 300 μl of methanol in a 5-ml centrifugation tube and centrifuged at 3000$g$ for 10 min. The supernatant layer was collected, and a 20-μl aliquot was injected for LC-MS/MS analysis. Standard curves for **5i3** in blood were generated by adding various concentrations of **5i3** together with an internal standard to blank plasma. Then, all samples were quantified with an Agilent 1200 LC/MSD (Agilent, USA). The mobile phase was methanol/1.5% glacial acetic acid (50/50, v/v) at a flow rate of 1.0 ml/min, and the test wavelength was 225 nm. All blood samples were centrifuged in an Eppendorf 5415D centrifuge and quantified by Agilent 1200 LC/MSD (Agilent, USA).

## Supplementary Materials

**This PDF file includes:**
Supplementary Material and Methods
Figs. S1 to S10
Tables S1 to S13

## REFERENCES AND NOTES

1. The Lancet HIV, UNAIDS strategy aligns HIV priorities with development goals. *Lancet HIV* **8**, e245 (2021).
2. A. S. Fauci, H. C. Lane, Four decades of HIV/AIDS—Much accomplished, much to do. *N. Engl. J. Med.* **383**, 1–4 (2020).
3. C. Beyrer, A. Pozniak, HIV drug resistance—An emerging threat to epidemic control. *N. Engl. J. Med.* **377**, 1605–1607 (2017).
4. M. Li, D. Oliveira Passos, Z. Shan, S. J. Smith, Q. Sun, A. Biswas, I. Choudhuri, T. S. Strutzenberg, A. Haldane, N. Deng, Z. Li, X. Z. Zhao, L. Briganti, M. Kvaratskhelia, T. R. Burke Jr., R. M. Levy, S. H. Hughes, R. Craigie, D. Lyumkis, Mechanisms of HIV-1 integrase resistance to dolutegravir and potent inhibition of drug-resistant variants. *Sci. Adv.* **9**, eadg5953 (2023).
5. A. Engelman, P. Cherepanov, The structural biology of HIV-1: Mechanistic and therapeutic insights. *Nat. Rev. Microbiol.* **10**, 279–290 (2012).
6. K. P. Larsen, Y. K. Mathiharan, K. Kappel, A. T. Coey, D. H. Chen, D. Barrero, L. Madigan, J. D. Puglisi, G. Skiniotis, E. V. Puglisi, Architecture of an HIV-1 reverse transcriptase initiation complex. *Nature* **557**, 118–122 (2018).
7. R. C. Burdick, R. Morse, I. Rouzina, M. C. Williams, W. S. Hu, V. K. Pathak, HIV-1 uncoating requires long double-stranded reverse transcription products. *Sci. Adv.* **10**, eadn7033 (2024).
8. K. Das, S. E. Martinez, J. J. DeStefano, E. Arnold, Structure of HIV-1 RT/dsRNA initiation complex prior to nucleotide incorporation. *Proc. Natl. Acad. Sci. U.S.A.* **116**, 7308–7313 (2019).
9. L. Tian, M. S. Kim, H. Li, J. Wang, W. Yang, Structure of HIV-1 reverse transcriptase cleaving RNA in an RNA/DNA hybrid. *Proc. Natl. Acad. Sci. U.S.A.* **115**, 507–512 (2018).
10. Z. Wang, S. Cherukupalli, M. Xie, W. Wang, X. Jiang, R. Jia, C. Pannecouque, E. De Clercq, D. Kang, P. Zhan, X. Liu, Contemporary medicinal chemistry strategies for the discovery and development of novel HIV-1 non-nucleoside reverse transcriptase inhibitors. *J. Med. Chem.* **65**, 3729–3757 (2022).
11. M. E. Cilento, K. A. Kirby, S. G. Sarafianos, Avoiding drug resistance in HIV reverse transcriptase. *Chem. Rev.* **121**, 3271–3296 (2021).
12. L. Ding, L. Zhuang, F. Chen, Druggability modification strategies of the diarylpyrimidine-type non-nucleoside reverse transcriptase inhibitors. *Med. Res. Rev.* **41**, 1255–1290 (2021).
13. HIV Drug Resistance Database; https://hivdb.stanford.edu.
14. V. Namasivayam, M. Vanangamudi, V. G. Kramer, S. Kurup, P. Zhan, X. Liu, J. Kongsted, S. N. Byrareddy, The journey of HIV-1 non-nucleoside reverse transcriptase inhibitors (NNRTIs) from lab to clinic. *J. Med. Chem.* **62**, 4851–4883 (2019).
15. Y. Ma, E. Frutos-Beltrán, D. Kang, C. Pannecouque, E. De Clercq, L. Menéndez-Arias, X. Liu, P. Zhan, Medicinal chemistry strategies for discovering antivirals effective against drug-resistant viruses. *Chem. Soc. Rev.* **50**, 4514–4540 (2021).
16. M. Aoki, H. Aoki-Ogata, H. Bulut, H. Hayashi, N. Takamune, N. Kishimoto, H. Tanaka, N. Higashi-Kuwata, S. I. Hattori, D. Das, K. Venkateswara Rao, K. Iwama, D. A. Davis, K. Hasegawa, K. Murayama, R. Yarchoan, A. K. Ghosh, A. K. Pau, S. Machida, S. Misumi, H. Mitsuya, GRL-142 binds to and impairs HIV-1 integrase nuclear localization signal and potently suppresses highly INSTI-resistant HIV-1 variants. *Sci. Adv.* **9**, eadg2955 (2023).
17. Y. Hsiou, J. Ding, K. Das, A. D. Clark Jr., P. L. Boyer, P. Lewi, P. A. Janssen, J. P. Kleim, M. Rösner, S. H. Hughes, E. Arnold, The Lys103Asn mutation of HIV-1 RT: A novel mechanism of drug resistance. *J. Mol. Biol.* **309**, 437–445 (2001).
18. K. Das, J. D. Bauman, A. D. Clark Jr., Y. V. Frenkel, P. J. Lewi, A. J. Shatkin, S. H. Hughes, E. Arnold, High-resolution structures of HIV-1 reverse transcriptase/TMC278 complexes: Strategic flexibility explains potency against resistance mutations. *Proc. Natl. Acad. Sci. U.S.A.* **105**, 1466–1471 (2008).
19. K. Singh, B. Marchand, D. K. Rai, B. Sharma, E. Michailidis, E. M. Ryan, K. B. Matzek, M. D. Leslie, A. N. Hagedorn, Z. Li, P. R. Norden, A. Hachiya, M. A. Parniak, H. T. Xu, M. A. Wainberg, S. G. Sarafianos, Biochemical mechanism of HIV-1 resistance to rilpivirine. *J. Biol. Chem.* **287**, 38110–38123 (2012).
20. Y. Yang, D. Kang, L. A. Nguyen, Z. B. Smithline, C. Pannecouque, P. Zhan, X. Liu, T. A. Steitz, Structural basis for potent and broad inhibition of HIV-1 RT by thiophene[3,2-*d*] pyrimidine non-nucleoside inhibitors. *eLife* **7**, e36340 (2018).
21. J. Ren, D. K. Stammers, Structural basis for drug resistance mechanisms for non-nucleoside inhibitors of HIV reverse transcriptase. *Virus Res.* **134**, 157–170 (2008).
22. J. Ren, D. K. Stammers, HIV reverse transcriptase structures: Designing new inhibitors and understanding mechanisms of drug resistance. *Trends Pharmacol. Sci.* **26**, 4–7 (2005).
23. A. E. Basson, S. Y. Rhee, C. M. Parry, Z. El-Khatib, S. Charalambous, T. De Oliveira, D. Pillay, C. Hoffmann, D. Katzenstein, R. W. Shafer, L. Morris, Impact of drug resistance-associated amino acid changes in HIV-1 subtype C on susceptibility to newer nonnucleoside reverse transcriptase inhibitors. *Antimicrob. Agents Chemother.* **59**, 960–971 (2015).
24. L. Tambuyzer, H. Azijn, L. T. Rimsky, J. Vingerhoets, P. Lecocq, G. Kraus, G. Picchio, M. P. de Béthune, Compilation and prevalence of mutations associated with resistance to non-nucleoside reverse transcriptase inhibitors. *Antivir. Ther.* **14**, 103–109 (2009).
25. W. T. Gray, K. M. Frey, S. B. Laskey, A. C. Mislak, K. A. Spasov, W. G. Lee, M. Bollini, R. F. Siliciano, W. L. Jorgensen, K. S. Anderson, Potent inhibitors active against HIV reverse transcriptase with K101P, a mutation conferring rilpivirine resistance. *ACS Med. Chem. Lett.* **6**, 1075–1079 (2015).
26. G. L. Melikian, S. Y. Rhee, V. Varghese, D. Porter, K. White, J. Taylor, W. Towner, P. Troia, J. Burack, E. Dejesus, G. K. Robbins, K. Razzeca, R. Kagan, T. F. Liu, W. J. Fessel, D. Israelski, R. W. Shafer, Non-nucleoside reverse transcriptase inhibitor (NNRTI) cross-resistance: Implications for preclinical evaluation of novel NNRTIs and clinical genotypic resistance testing. *J. Antimicrob. Chemother.* **69**, 12–20 (2014).
27. M.-T. Lai, V. Munshi, M. Lu, M. Feng, R. Hrin-Solt, P. M. McKenna, D. J. Hazuda, M. D. Miller, Mechanistic study of common non-nucleoside reverse transcriptase inhibitor-resistant mutations with K103N and Y181C substitutions. *Viruses* **8**, 263 (2016).

28. C. Soulie, M. M. Santoro, C. Charpentier, A. Storto, D. Paraskevis, D. Di Carlo, W. Gennari, G. Sterrantino, M. Zazzi, C. F. Perno, V. Calvez, D. Descamps, F. Ceccherini-Silberstein, A. G. Marcelin, Rare occurrence of doravirine resistance-associated mutations in HIV-1-infected treatment-naive patients. *J. Antimicrob. Chemother.* **74**, 614–617 (2019).

29. C. Soulie, M. M. Santoro, A. Storto, B. Abdi, C. Charpentier, D. Armenia, A. Jary, F. Forbici, A. Bertoli, W. Gennari, M. Andreoni, C. Mussini, A. Antinori, C. F. Perno, V. Calvez, F. Ceccherini-Silberstein, D. Descamps, A. G. Marcelin, Prevalence of doravirine-associated resistance mutations in HIV-1-infected antiretroviral-experienced patients from two large databases in France and Italy. *J. Antimicrob. Chemother.* **75**, 1026–1030 (2020).

30. B. G. Brenner, M. Oliveira, R. I. Ibanescu, J. P. Routy, R. Thomas, Doravirine responses to HIV-1 viruses bearing mutations to NRTIs and NNRTIs under in vitro selective drug pressure. *J. Antimicrob. Chemother.* **78**, 1921–1928 (2023).

31. S. Gallien, I. Charreau, M. L. Nere, N. Mahjoub, F. Simon, N. de Castro, J. P. Aboulker, J. M. Molina, C. Delaugerre, Archived HIV-1 DNA resistance mutations to rilpivirine and etravirine in successfully treated HIV-1-infected individuals pre-exposed to efavirenz or nevirapine. *J. Antimicrob. Chemother.* **70**, 562–565 (2015).

32. T. Diphoko, S. Gaseitsiwe, I. Kasvosve, S. Moyo, H. Okatch, R. Musonda, M. Wainberg, J. Makhema, R. Marlink, V. Novitsky, M. Essex, Prevalence of rilpivirine and etravirine resistance mutations in HIV-1 subtype C-infected patients failing nevirapine or efavirenz-based combination antiretroviral therapy in Botswana. *AIDS Res. Hum. Retroviruses* **34**, 667–671 (2018).

33. D. M. Himmel, E. Arnold, Non-nucleoside reverse transcriptase inhibitors join forces with integrase inhibitors to combat HIV. *Pharmaceuticals (Basel)* **13**, 122 (2020).

34. H. Azijn, I. Tirry, J. Vingerhoets, M.-P. de Béthune, G. Kraus, K. Boven, D. Jochmans, E. Van Craenenbroeck, G. Picchio, L. T. Rimsky, TMC278, a next-generation nonnucleoside reverse transcriptase inhibitor (NNRTI), active against wild-type and NNRTI-resistant HIV-1. *Antimicrob. Agents Chemother.* **54**, 718–727 (2010).

35. S. Gupta, S. Fransen, E. E. Paxinos, E. Stawiski, W. Huang, C. J. Petropoulos, Combinations of mutations in the connection domain of human immunodeficiency virus type 1 reverse transcriptase: Assessing the impact on nucleoside and nonnucleoside reverse transcriptase inhibitor resistance. *Antimicrob. Agents Chemother.* **54**, 1973–1980 (2010).

36. D. Kang, Z. Fang, Z. Li, B. Huang, H. Zhang, X. Lu, H. Xu, Z. Zhou, X. Ding, D. Daelemans, E. De Clercq, C. Pannecouque, P. Zhan, X. Liu, Design, synthesis, and evaluation of thiophene[3,2-d]pyrimidine derivatives as HIV-1 non-nucleoside reverse transcriptase inhibitors with significantly improved drug resistance profiles. *J. Med. Chem.* **59**, 7991–8007 (2016).

37. D. Kang, Z. Fang, B. Huang, X. Lu, H. Zhang, H. Xu, Z. Huo, Z. Zhou, Z. Yu, Q. Meng, G. Wu, X. Ding, Y. Tian, D. Daelemans, E. De Clercq, C. Pannecouque, P. Zhan, X. Liu, Structure-based optimization of thiophene[3,2-d]pyrimidine derivatives as potent HIV-1 non-nucleoside reverse transcriptase inhibitors with improved potency against resistance-associated variants. *J. Med. Chem.* **60**, 4424–4443 (2017).

38. M. C. Sanguinetti, M. Tristani-Firouzi, hERG potassium channels and cardiac arrhythmia. *Nature* **440**, 463–469 (2006).

39. S. Kalyaanamoorthy, K. H. Barakat, Development of safe drugs: The hERG challenge. *Med. Res. Rev.* **38**, 525–555 (2018).

40. X. Jiang, J. Yu, Z. Zhou, J. Kongsted, Y. Song, C. Pannecouque, E. De Clercq, D. Kang, V. Poongavanam, X. Liu, P. Zhan, Molecular design opportunities presented by solvent-exposed regions of target proteins. *Med. Res. Rev.* **39**, 2194–2238 (2019).

41. S. Agnello, M. Brand, M. F. Chellat, S. Gazzola, R. Riedl, A structural view on medicinal chemistry strategies against drug resistance. *Angew. Chem. Int. Ed. Engl.* **58**, 3300–3345 (2019).

42. G. Wu, T. Zhao, D. Kang, J. Zhang, Y. Song, V. Namasivayam, J. Kongsted, C. Pannecouque, E. De Clercq, V. Poongavanam, X. Liu, P. Zhan, Overview of recent strategic advances in medicinal chemistry. *J. Med. Chem.* **62**, 9375–9414 (2019).

43. L. Ding, C. Pannecouque, E. De Clercq, C. Zhuang, F. E. Chen, Discovery of novel pyridine-dimethyl-phenyl-DAPY hybrids by molecular fusing of methyl-pyrimidine-DAPYs and difluoro-pyridinyl-DAPYs: Improving the druggability toward high inhibitory activity, solubility, safety, and PK. *J. Med. Chem.* **65**, 2122–2138 (2022).

44. X. Jin, L. M. Zhao, S. Wang, W. J. Huang, Y. X. Zhang, C. Pannecouque, E. De Clercq, F. E. Chen, Structure-based discovery of novel NH$_2$-biphenyl-diarylpyrimidines as potent non-nucleoside reverse transcriptase inhibitors with significantly improved safety: From NH$_2$-naphthyl-diarylpyrimidine to NH$_2$-biphenyl-diarylpyrimidine. *J. Med. Chem.* **65**, 8478–8492 (2022).

45. N. Sluis-Cremer, Future of nonnucleoside reverse transcriptase inhibitors. *Proc. Natl. Acad. Sci. U.S.A.* **115**, 637–638 (2018).

46. D. G. Kuroda, J. D. Bauman, J. R. Challa, D. Patel, T. Troxler, K. Das, E. Arnold, R. M. Hochstrasser, Snapshot of the equilibrium dynamics of a drug bound to HIV-1 reverse transcriptase. *Nat. Chem.* **5**, 174–181 (2013).

47. D. Liebschner, P. V. Afonine, N. W. Moriarty, B. K. Poon, O. V. Sobolev, T. C. Terwilliger, P. D. Adams, Polder maps: Improving OMIT maps by excluding bulk solvent. *Acta Crystallogr. D Struct. Biol.* **73**, 148–157 (2017).

48. D. Kang, F. X. Ruiz, Y. Sun, D. Feng, L. Jing, Z. Wang, T. Zhang, S. Gao, L. Sun, E. De Clercq, C. Pannecouque, E. Arnold, P. Zhan, X. Liu, 2,4,5-trisubstituted pyrimidines as potent HIV-1 NNRTIs: Rational design, synthesis, activity evaluation, and crystallographic studies. *J. Med. Chem.* **64**, 4239–4256 (2021).

49. T. Lynch, A. Price, The effect of cytochrome P450 metabolism on drug response, interactions, and adverse effects. *Am. Fam. Physician* **76**, 391–396 (2007).

50. F. P. Guengerich, Cytochrome P450 research and *The Journal of Biological Chemistry*. *J. Biol. Chem.* **294**, 1671–1680 (2019).

51. J. P. Havens, A. T. Podany, K. K. Scarsi, C. V. Fletcher, Clinical pharmacokinetics and pharmacodynamics of etravirine: An updated review. *Clin. Pharmacokinet.* **59**, 137–154 (2020).

52. J. S. Mitcheson, J. Chen, M. Lin, C. Culberson, M. C. Sanguinetti, A structural basis for drug-induced long QT syndrome. *Proc. Natl. Acad. Sci. U.S.A.* **97**, 12329–12333 (2000).

53. G. Gintant, P. T. Sager, N. Stockbridge, Evolution of strategies to improve preclinical cardiac safety testing. *Nat. Rev. Drug Discov.* **15**, 457–471 (2016).

54. E. De Clercq, G. Li, Approved antiviral drugs over the past 50 years. *Clin. Microbiol. Rev.* **29**, 695–747 (2016).

55. W. L. Jorgensen, Efficient drug lead discovery and optimization. *Acc. Chem. Res.* **42**, 724–733 (2009).

56. Z. G. Bowe, S. Shanmugam, H. Hall-Thomsen, S. I. Gubernick, The landscape and market for HIV therapies. *Nat. Rev. Drug Discov.* **23**, 334–335 (2024).

57. B. J. van Welzen, S. F. L. Van Lelyveld, G. Ter Beest, J. H. Gisolf, S. E. Geerlings, J. M. Prins, G. Van Twillert, C. Van Nieuwkoop, M. Van der Valk, D. Burger, A. M. J. Wensing, Virological failure after switch to long-acting cabotegravir and rilpivirine injectable therapy: An in-depth analysis. *Clin. Infect. Dis.* **79**, 189–195 (2024).

58. V. Poongavanam, V. Namasivayam, M. Vanangamudi, H. Al Shamaileh, R. N. Veedu, J. Kihlberg, N. A. Murugan, Integrative approaches in HIV-1 non-nucleoside reverse transcriptase inhibitor design. *Wiley Interdiscip. Rev. Comput. Mol. Sci.* **8**, e1328 (2018).

59. K. Das, A. D. Clark Jr., P. J. Lewi, J. Heeres, M. R. De Jonge, L. M. Koymans, H. M. Vinkers, F. Daeyaert, D. W. Ludovici, M. J. Kukla, B. De Corte, R. W. Kavash, C. Y. Ho, H. Ye, M. A. Lichtenstein, K. Andries, R. Pauwels, M. P. De Bethune, P. L. Boyer, P. Clark, S. H. Hughes, P. A. Janssen, E. Arnold, Roles of conformational and positional adaptability in structure-based design of TMC125-R165335 (etravirine) and related non-nucleoside reverse transcriptase inhibitors that are highly potent and effective against wild-type and drug-resistant HIV-1 variants. *J. Med. Chem.* **47**, 2550–2560 (2004).

60. Z. Dang, W. Lai, K. Qian, P. Ho, K. H. Lee, C. H. Chen, L. Huang, Betulinic acid derivatives as human immunodeficiency virus type 2 (HIV-2) inhibitors. *J. Med. Chem.* **52**, 7887–7891 (2009).

61. N. Liu, L. Wei, L. Huang, F. Yu, W. Zheng, B. Qin, D. Q. Zhu, S. L. Morris-Natschke, S. Jiang, C. H. Chen, K. H. Lee, L. Xie, Novel HIV-1 non-nucleoside reverse transcriptase inhibitor agents: Optimization of diarylanilines with high potency against wild-type and rilpivirine-resistant E138K mutant virus. *J. Med. Chem.* **59**, 3689–3704 (2016).

62. D. Kang, H. Zhang, Z. Wang, T. Zhao, T. Ginex, F. J. Luque, Y. Yang, G. Wu, D. Feng, F. Wei, J. Zhang, E. De Clercq, C. Pannecouque, C. H. Chen, K. H. Lee, N. A. Murugan, T. A. Steitz, P. Zhan, X. Liu, Identification of dihydrofuro[3,4-d]pyrimidine derivatives as novel HIV-1 non-nucleoside reverse transcriptase inhibitors with promising antiviral activities and desirable physicochemical properties. *J. Med. Chem.* **62**, 1484–1501 (2019).

63. A. Hombrouck, A. Voet, B. Van Remoortel, C. Desadeleer, M. De Maeyer, Z. Debyser, M. Witvrouw, Mutations in human immunodeficiency virus type 1 integrase confer resistance to the naphthyridine L-870,810 and cross-resistance to the clinical trial drug GS-9137. *Antimicrob. Agents Chemother.* **52**, 2069–2078 (2008).

64. J. Snoeck, C. Riva, K. Steegen, Y. Schrooten, B. Maes, K. Vergne, K. Van Laethem, M. Peeters, A. M. Vandamme, Optimization of a genotypic assay applicable to all human immunodeficiency virus type 1 protease and reverse transcriptase subtypes. *J. Virol. Methods* **128**, 47–53 (2005).

65. B. Vrancken, N. S. Trovão, G. Baele, E. van Wijngaerden, A.-M. Vandamme, K. van Laethem, P. Lemey, Quantifying next generation sequencing sample pre-processing bias in HIV-1 complete genome sequencing. *Viruses* **8**, 12 (2016).

66. R. Pauwels, J. Balzarini, M. Baba, R. Snoeck, D. Schols, P. Herdewijn, J. Desmyter, E. De Clercq, Rapid and automated tetrazolium-based colorimetric assay for the detection of anti-HIV compounds. *J. Virol. Methods* **20**, 309–321 (1988).

67. C. Pannecouque, D. Daelemans, E. De Clercq, Tetrazolium-based colorimetric assay for the detection of HIV replication inhibitors: Revisited 20 years later. *Nat. Protoc.* **3**, 427–434 (2008).

68. J. D. Bauman, K. Das, W. C. Ho, M. Baweja, D. M. Himmel, A. D. Clark Jr., D. A. Oren, P. L. Boyer, S. H. Hughes, A. J. Shatkin, E. Arnold, Crystal engineering of HIV-1 reverse transcriptase for structure-based drug design. *Nucleic Acids Res.* **36**, 5083–5092 (2008).

69. Z. Otwinowski, W. Minor, Processing of X-ray diffraction data collected in oscillation mode. *Methods Enzymol.* **276**, 307–326 (1997).

70. P. D. Adams, P. V. Afonine, G. Bunkóczi, V. B. Chen, I. W. Davis, N. Echols, J. J. Headd, L.-W. Hung, G. J. Kapral, R. W. Grosse-Kunstleve, A. J. McCoy, N. W. Moriarty, R. Oeffner, R. J. Read, D. C. Richardson, J. S. Richardson, T. C. Terwilliger, P. H. Zwart, *PHENIX*: A

comprehensive Python-based system for macromolecular structure solution. *Acta Crystallogr. D Biol. Crystallogr.* **66**, 213–221 (2010).

71. P. Emsley, K. Cowtan, Coot: Model-building tools for molecular graphics. *Acta Crystallogr. D Biol. Crystallogr.* **60**, 2126–2132 (2004).

72. R. Fährrolfes, S. Bietz, F. Flachsenberg, A. Meyder, E. Nittinger, T. Otto, A. Volkamer, M. Rarey, Proteins*Plus*: A web portal for structure analysis of macromolecules. *Nucleic Acids Res.* **45**, W337–W343 (2017).

73. F. Flachsenberg, A. Meyder, K. Sommer, P. Penner, M. Rarey, A consistent scheme for gradient-based optimization of protein-ligand poses. *J. Chem. Inf. Model.* **60**, 6502–6522 (2020).

74. R. H. B. Smith, A. C. Dar, A. Schlessinger, PyVOL: A PyMOL plugin for visualization, comparison, and volume calculation of drug-binding sites. bioRxiv 816702 [Preprint] (2019). https://doi.org/10.1101/816702.

75. A. Daina, O. Michielin, V. Zoete, SwissADME: A free web tool to evaluate pharmacokinetics, drug-likeness and medicinal chemistry friendliness of small molecules. *Sci. Rep.* **7**, 42717 (2017).